Inclusive Polarized Structure Functions g_1^p and g_1^d from the eg1-DVCS experiment

P.E. Bosted, N. Kvaltine, Y. Prok, *

(Dated: September 25, 2013)

Abstract

The inclusive polarized structure functions of the proton and deuteron, g_1^p and g_1^d, were measured with high statistical accuracy using polarized 6 GeV electrons incident on a 2.5% r.l. polarized ammonia target in Hall B at Jefferson Lab. Electrons scattered at lab angles between 18 and 45 degrees were detected in the CLAS. For DIS kinematics $Q^2 > 1$ GeV^2 and $W > 2$ GeV, the ratio of polarized to unpolarized structure functions g_1/F_1 is found to be nearly independent of Q^2. In the framework of pQCD, these results can be used to better constrain the polarization of quarks and gluons in the nucleon, as well as higher-twist contributions.

PACS numbers: 13.60.Hb, 13.88.+e , 14.20.Dh

*Electronic address: `bosted@jlab.org,kvaltine@jlab.org,yprok@jlab.org`

Contents

I. INTRODUCTION

A full understanding of the spin structure of the nucleon (and determination of the polarized gluon density $\Delta G(x)$ in particular) is a major goal of particle/nuclear physics. Deep-inelastic lepton scattering from nucleons has proved over the years to be the cleanest tool to study the short-distance structure of the nucleon. The pioneering experiments at SLAC, followed by several generations of experiments at FermiLab, SLAC, CERN, DESY, and elsewhere, have made great strides in determining the spin-averaged parton densities of the quarks and gluons in the proton and neutron. Starting in the 1970's, experiments using polarized targets have been making steady progress in determining the spin-dependent longitudinal parton densities, although over a more restricted range in momentum fraction x and momentum transfer squared Q^2 due to the lower luminosity available with polarized targets. Initial studies from SLAC and CERN, borne out with increased precision with subsequent experiments at SLAC [1, 2], CERN [4], DESY [3], JLab [5, 6] and elsewhere, showed that the up and down quark helicities sum to only a small fraction of total spin of the nucleon, in the framework of the Standard Model and pQCD. This implies that the net contribution of polarized gluons, strange quarks, and parton angular momentum must be substantial.

Specifically concerning the gluon spin, there are two approaches that are being followed. The first is to try to isolate specific processes in which a polarized gluon is involved at leading order, for example photon-gluon fusion leading to a pair of charmed quarks (COMPASS)[4], or quark-gluon scattering leading to a high energy photon (RHIC-spin). The interpretation of these interactions is complicated due both to background events (other tree-level process that can lead to the same final state) and higher order QCD corrections.

A theoretically cleaner approach is to examine the Q^2 dependence of the spin structure function g_1. Perturbative QCD allows a simple expression of g_1 in terms of the quark and gluon distributions Δq, $\Delta\overline{q}$ and ΔG, which evolve according to the DGLAP equations [7] due to gluon radiation:

$$g_1(x,Q^2)_{\rm pQCD} = \frac{1}{2}\sum e_q^2 \left[(\Delta q + \Delta\overline{q}) \otimes \left(1 + \frac{\alpha_s(Q^2)}{2\pi}\delta C_q\right) + \frac{\alpha_s(Q^2)}{2\pi}\Delta G \otimes \frac{\delta C_G}{N_f}\right]. \quad (1)$$

where α_s is the strong coupling factor, δC_q and δC_G are the Wilson coefficients, and N_f is the number of quark flavors.

In practice, fits to data should include the effects of both kinematic and dynamic higher twist. This quantities are of increasing theoretical interest in their own right. In the spin-averaged case, pQCD evolution is the bench-mark approach to which reaction-specific determinations of the gluon density $G(x)$ are compared. This is possible due to the high accuracy of measurements of the spin-averaged structure function F_2 over many decades in both x and Q^2 (needed because the evolution due to gluon radiation is essentially logarithmic in nature). In the polarized case, the kinematic range of present precise data [1–4] is considerably more limited. Nonetheless, the data are of sufficient quality to obtain a very good description of the valence up and down quark polarizations, and rough indications of the gluon and sea quark polarizations..

The goal of the present analysis is to provide much higher statistical precision in measurements of g_1^p and g_1^d than was previously available in the limited kinematic range accessible with 6 GeV electrons at Jefferson Lab. This precision is needed to distinguish between power-law higher-twist contributions and logarithmic gluon radiation contributions, especially when combined with planned data with 11 GeV electrons.

A. Experimental context

CLAS has been used to measure the inclusive polarized structure functions of the proton (g_1^p) and deuteron (g_1^d) on several occasions prior to the present experiment (dubbed "eg1-dvcs"). The results from the data taking in 1998 ("eg1a") and in 2000 ("eg1b") have been reviewed and published [5, 6]. Detailed archival papers for eg1b are being written. The eg4 experiment, which ran from January to May 2006, is still under analysis. All the experiments, including eg1-dvcs, used the same polarized ammonia target [8]. Eg1a and eg1b used a wide range of beam energies (from 1.7 to 5.7 GeV) to cover a large kinematic range, from the nucleon resonance region to deep-inelastic scattering (DIS) region. Eg4 used lower beam energies and focused on very forward scattering angles to focus on the resonance region at low Q^2. The present experiment used only 6 GeV electrons (except for 4 days at 4.8 GeV) and relatively larger scattering angles to focus on the DIS region. The main focus of eg1-dvcs was on semi-inclusive DIS (SIDIS) and deeply virtual Compton scattering (DVCS), both of which required detection of photons at small angles. For this reason, an Inner Calorimeter (IC) was installed. This detector blocked scattered electrons below about 17 degrees. The IC is not used in the present inclusive analysis.

The present analysis closely follows those of eg1a and eg1b. Small differences result from the use of $^{14}NH_3$ instead of $^{15}NH_3$, a 50% longer target cell, the inclusion of the IC detector into CLAS, and a more careful treatment of the effects of the polarized target magnetic field. Parallel analyses were done by P. Bosted and Y. Prok for the proton section of eg1-dvcs, and P. Bosted and N. Kvaltine for the deuteron section.

The eg1-dvcs experiment comprises many different physics analyses, most of which have many features in common. These include information on the beam and target parameters, improvements to data processing, and data quality checks. Most of these features are detailed in eg1-dvcs Technical Notes, which are referenced throughout this document.

B. Experimental overview

The "eg1-dvcs" experiment used 6 GeV longitudinally polarized electrons from CEBAF at Jefferson Lab impinging on a 0.025 r.l. longitudinally polarized solid ammonia target immersed in liquid helium [8, 9]. Inclusive scattered electrons were detected in the CEBAF Large Acceptance Spectrometer (CLAS) [10]. The typical beam current was 7 nA, which, when integrated over the 5 months of data taking with 40% 'overall 'production" data taking efficiency, resulted in approximately 2.5×10^{17} electrons traversing the ammonia targets. The beam polarization, as periodically measured using Møller scattering in an upstream polarimeter, averaged 85% for the first three quarters of the experiment. A lower polarization of about 75% was delivered during the remaining time, in order to accommodate the needs of Hall A and Hall C.

About 70% of the running time was on polarized protons (NH_3 target), 20% on polarized deuterons (ND_3 target), 10% on a reference unpolarized carbon target, and 1% on an empty cell. The 1.5-cm-diameter cups typically contained 1 g/cm^2 of material immersed in a 2-cm-long liquid helium bath. In order to depolarize the target as slowly as possible, the sub-millimeter-diameter beam was uniformly rastered over the front face of the target every few seconds. The beam position, averaged over a few minutes or longer, was kept stable at the 0.1 mm level, using feedback from a set of beam position monitors. A split solenoid superconducting magnet provided a highly uniform 5 T magnetic field near the target, which effectively extended about 20 cm upstream and downstream of the target center.

Scattered electrons were detected in the CLAS detector [10] in Hall B, over polar angles from 17 to 48 degrees. CLAS comprises six azimuthally symmetric detector arrays embedded in a toroidal magnetic field. Particle momenta and scattering angles were measured with the drift chamber (DC) tracking system to a relative accuracy of 0.3% to 2% in momentum, and about 1 mr in angle. Electrons were separated from a significantly larger flux of charged pions using segmented gas Cherenkov detectors (pion threshold 2.6 GeV) and an electromagnetic calorimeter. In order to not overwhelm the data acquisition system, the hardware trigger system rejected about 90% of pions while keeping close to 99% of electrons. The hardware Cherenkov and calorimeter thresholds were adjusted to give a trigger rate of about 3000 Hz, with a dead time of about 10%. An additional unbiased trigger, prescaled by a large factor, was used to measure the efficiency of the main electron trigger.

The data taking was divided into three parts: Part A in early 2009 used an NH_3 target, centered at 58 cm upstream of CLAS center ($z_0 = -58$ cm); Part B (mid 2009) also used NH_3, this time at $z_0 = -68$ cm; and Part C (September 2009) used ND_3 and NH_3 as target, again with $z_0 = -68$ cm. Each part had slightly different primary beam energies (between 5.7 and 6.0 GeV, with several days at 4.8 GeV at the end of Part A). The CLAS torus polarity was set to bend electrons inwards for almost all of parts A and B, and about two thirds of Part C. The field strength was 2/3 of maximum (corresponding to a current of 2250 A).

The main difference between this experiment and previous CLAS runs with polarized ammonia targets was the addition of an Inner Calorimeter. Although not used in the present analysis, this device had the advantage of absorbing much of the background from Møller scattering, allowing for the use of higher beam currents than usual, but also had the disadvantage of blocking electrons below scattering angles of 20 (17) degrees for Part A (parts B and C). Other differences included the use of a 50% longer target cell and nitrogen-14 instead of nitrogen-15 in the ammonia.

name	beam energy	I torus
Part A (5.9)	5.9 GeV	2250 A
Part A (4.8)	4.8 GeV	2250 A
Part B (in)	5.9 GeV	2250 A
Part B (out)	5.9 GeV	-2250 A
Part C (in)	5.7 GeV	2250 A
Part C (out)	5.7 GeV	-2250 A

TABLE I: Names, nominal beam energy, and CLAS torus current of the different parts of the experiment, listed in the order of occurrence.

II. DATA PROCESSING

For the present analysis, the only particles of interest are scattered electrons. The spin structure functions were determined from the difference in rates in a particular x and Q^2 bin for beam and target polarizations aligned or anti-aligned. A large background of scattering from unpolarized (or slightly polarized) material in the target was taken into account using a detailed model of the target.

A. Data processing

The raw data consisted of approximately 50,000 files, each about 2 GB in size and corresponding to a few minutes of data taking. The files were grouped into runs consisting of about 80 files, on average, all with the same experimental configuration. Each file was processed with the standard CLAS analysis package. Several iterations occurred as calibrations were improved. The results in this analysis are from Pass 1, version 3 for Parts A and B, and version 5 for Part C. The extra two versions for part C were needed to correctly take into account the delayed helicity reporting for this run period. A subset of the processed data was stored on disk in both PAW ntuples and ROOT trees [15]. The subset included only events that were reasonably likely to have a scattered electron, since all analyses required this.

B. Post-processing

The processed data were corrected using an improved method of tracking particles through the target magnetic field. The standard method in RECSIS swims particles backwards to a plane perpendicular to the appropriate sector. Since eg1-dvcs is, in general, only looking for events with vertex positions in the target, a more accurate method is to swim the particle back to the x and y coordinates specified by the raster magnet. This method used the track coordinates at the first drift chamber layer and a fit to a large ensemble of simulated forward-swimming particles. This ensured that the track would intersect the beam line for a given raster magnet setting. The net result was about a factor of two improved angular resolution, as verified by the width of the beam energy, E_0, reconstructed from the electron and proton scattering angles in *ep* elastic scattering. Figure 1 show this improvement for all sectors (see Ref. [16]).

For Part C only, the beam helicity was not directly available for each event in the data stream. Instead, the information corresponded to that of the previous helicity bucket (a 1/30 sec time interval). The correct helicity information was obtained using two different schemes: 1) by making two passes through the data and making a look-up table; and 2) using the known pattern of helicity reversals, established by the first 32 helicity buckets in a given run. Except for two runs, we were able to reliably obtain the beam helicity for each event in Part C (see Ref. [17]).

C. Calibrations

1. Standard calibrations

Standard calibration procedures were done for each of the subsystems in CLAS. These included: drift chamber (DC) alignment using straight-through tracks [11]; DC timing alignments [12]; gas Cherenkov detector (CC) pulse height calibration using single photo-electron peak [13]; time-of-flight scintillator (SC) timing corrections; and electromagnetic calorimeter (EC) pulse height corrections using cosmic rays. Timing and position resolutions for each of the systems, after calibration, were similar to those obtained during other electron running periods [10]. Calibrations were made frequently enough to ensure very good stability for most of the systems. The exception was the EC gain, which varied substantially over a pe-

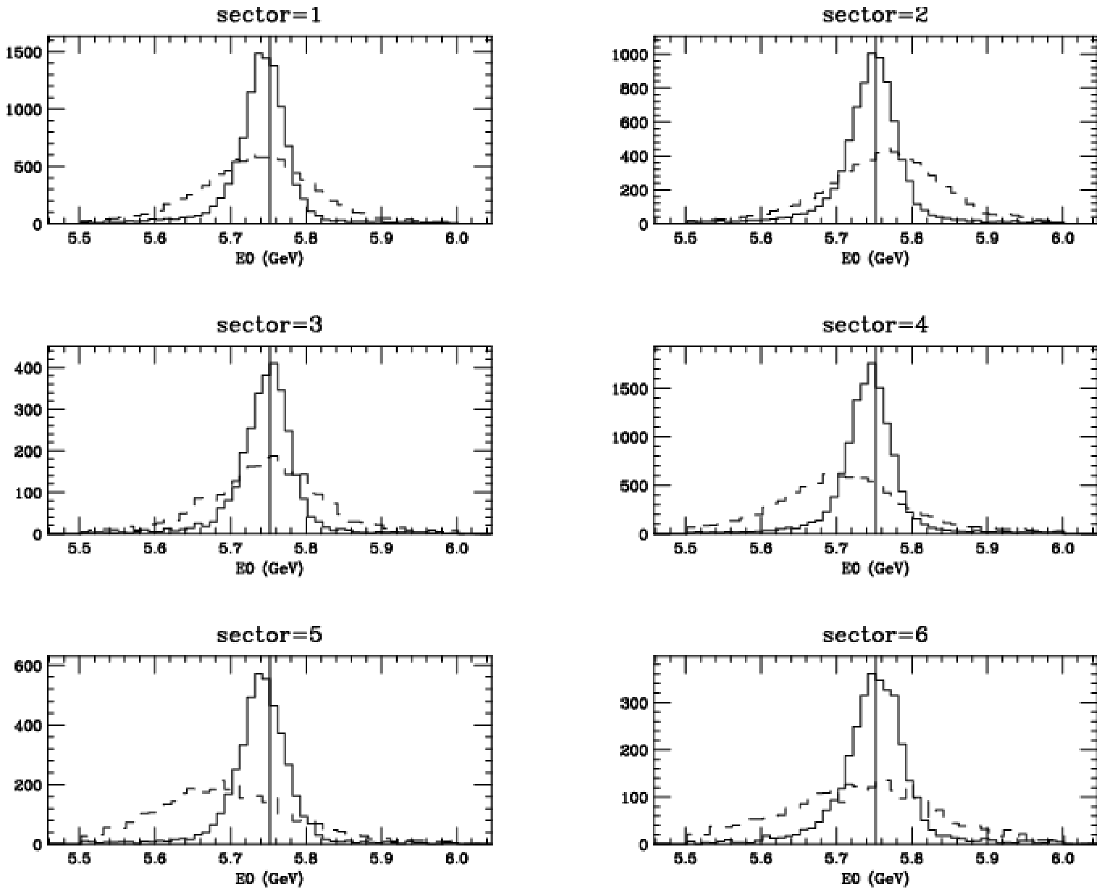

FIG. 1: Distribution of reconstructed beam energy E_0 by sector using elastic *ep* angles for a typical NH_3 run. Solid-line histograms use the new method to fit to a line while dashed-line histograms are from RECSIS swimming back to a plane. The lack of sector dependence of the peaks from the new method results from the correction for the target solenoid tilt.

riod of hours every time the high voltage to the photomultiplier tubes (PMTs) was turned off for a significant time. Whatever the cause, the gains of the PMTs in a given sector varied together in a highly correlated way, so that an overall gain adjustment on a run-by-run basis was adequate to obtain constant energy resolution and normalization.

2. Raster corrections

An additional calibration specific to experiments with polarized targets was done. This was to calibrate the beam position at the target, which depended on steering in the accelerator, as well as the strength of a set of deflection magnets used to raster the beam uniformly over the 1.5-cm-diameter target face once every few seconds [14]. The x and y magnet field (in units of ADC counts) was recorded for each event trigger. By minimizing the width of the reconstructed target position along the beam line (z), the relation between magnet current and beam position was determined, as well as the beam position relative to CLAS center for no raster magnet field. Also determined from the fit was the target center along the beam line relative to the center of CLAS. This was found to be -57.95 cm for Part A, and -67.95 cm for parts B and C of the run. These values are about 0.5 cm different than the physical survey values (see Ref. [14]). Since this discrepancy was observed in the previous polarized target experiment (eg1b), it is probably due to an error in the fiducial marks relating the target position to the vacuum vessel.

3. Magnet angle correction

Another calibration specific to this experiment was the determination of the orientation of the target solenoid with respect to the beam line. The primary method used was to make the opening angle of reconstructed electron-positron pairs (from photon conversions) as close to zero as possible. The result was an approximately 3 mr tilt, resulting in a significant polar deflection of charged particles, on top of the azimuthal rotation characteristic of a solenoidal field. The results were confirmed using the co-planarity of *ep* elastic events, and incorporated into the track reconstruction. The result of the correction can be seen in Fig. 1 by the reduced sector dependence of the peak (see Ref. [16]).

D. Event selection

In this experiment, the events of interest are those with at least one well-identified electron originating from the target. The two detectors used for particle ID were the threshold gas Cherenkov detector ("CC", with a pion threshold of 2.6 GeV) and the lead-scintillator electromagnetic calorimeter ("EC"), with a nominal sampling fraction of 0.30. The first level of selection was in the electron trigger, which required about 1 photo-electron (p.e.) in the CC and an energy deposition of 0.5 GeV in the EC.

In software, an electron was identified by requiring that a time-based drift-chamber ("DC") track have negative charge, using at least five of the six super-layers in the tracking system, and having a signal in each of the CC, EC, and scintillator time-of-flight counter system ("SC"). A further requirement was that the CLAS sector number for each the sub-systems (DC, CC, SC, and EC) had to match. We then required seven additional particle ID cuts, listed in order of effectiveness at removing background:

- The number of photo-electrons (p.e.) in the CC must be greater than 2.0 p.e. As illustrated in Fig. 2, this cut removes most of the background peak centered on 1 p.e. The background primarily originated from knock-on electrons from pions interacting in the Cherenkov window and gas medium.

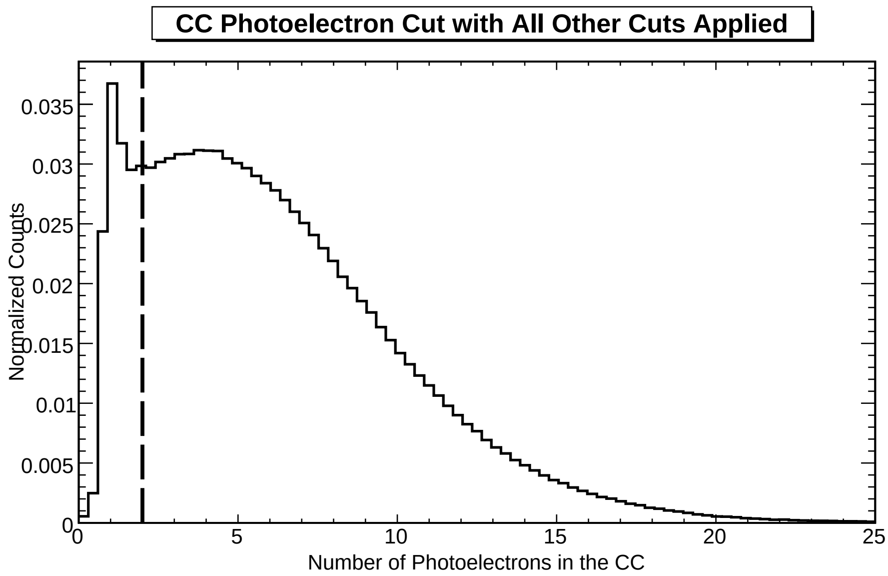

FIG. 2: Distribution of p.e. in the CC for events with all other electron cuts applied. The vertical line shows the cut value used in the analysis.

- The EC energy E divided by momentum P (with a 0.12 GeV offset) must be greater than 80% of the peak value of the distribution in a given sector, as determined from a first pass through the data. This procedure was performed to take out slow drifts in the EC gain, which were especially evident after the high voltage on the PMTs had been off for a significant period of time. The offset of 0.12 GeV was obtained from a fit to data with $1.2 < P < 5$ GeV, and can be attributed to energy loss in the detectors in front of the EC, as well as to the minimum ADC signal size used in the analysis. The effectiveness of this cut is illustrated in Fig. 3.

- Target vertex position along the beam line (z) must be within 3 cm of the polarized

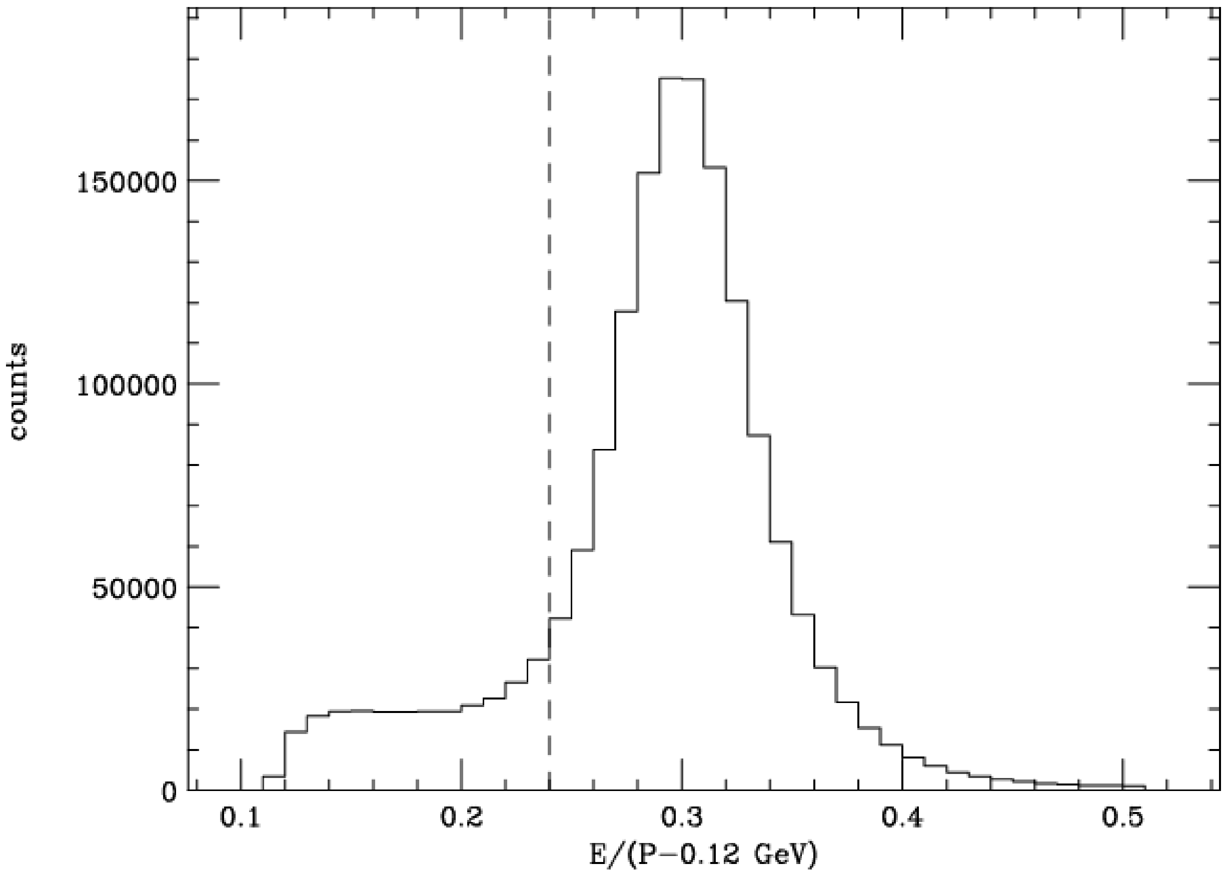

FIG. 3: Distribution of EC energy divided by track momentum (minus 0.12 GeV) for events with all other electron cuts applied. The vertical line shows the cut value used in the analysis.

target center, as illustrated in Fig. 4. The target is 1.5 cm long ($\pm$ 0.75cm from the beam center), while the resolution in vertex z varies between 0.3 and 0.6 cm depending on electron' momentum and angle, making the cut of $\pm$ 3.0 cm always greater than 3-σ from the end of the target. This cut removes the few percent of events originating from beam line materials such as vacuum windows and heat shields.

- Cherenkov mirror number must be aligned with the value expected from the track trajectory (as defined by the nearby SC paddle number) within two SC paddle numbers. For historical reasons, we use a quantity called Cherenkov χ^2 (C2), which is the squared angular difference in radians squared. The width of two SC paddles corresponds to our cut value of 0.05. The definition of C2 was modified from the one normally used, which was specifically designed for in-bending electrons from a target centered in CLAS, to work properly for any torus field and any target position [18].

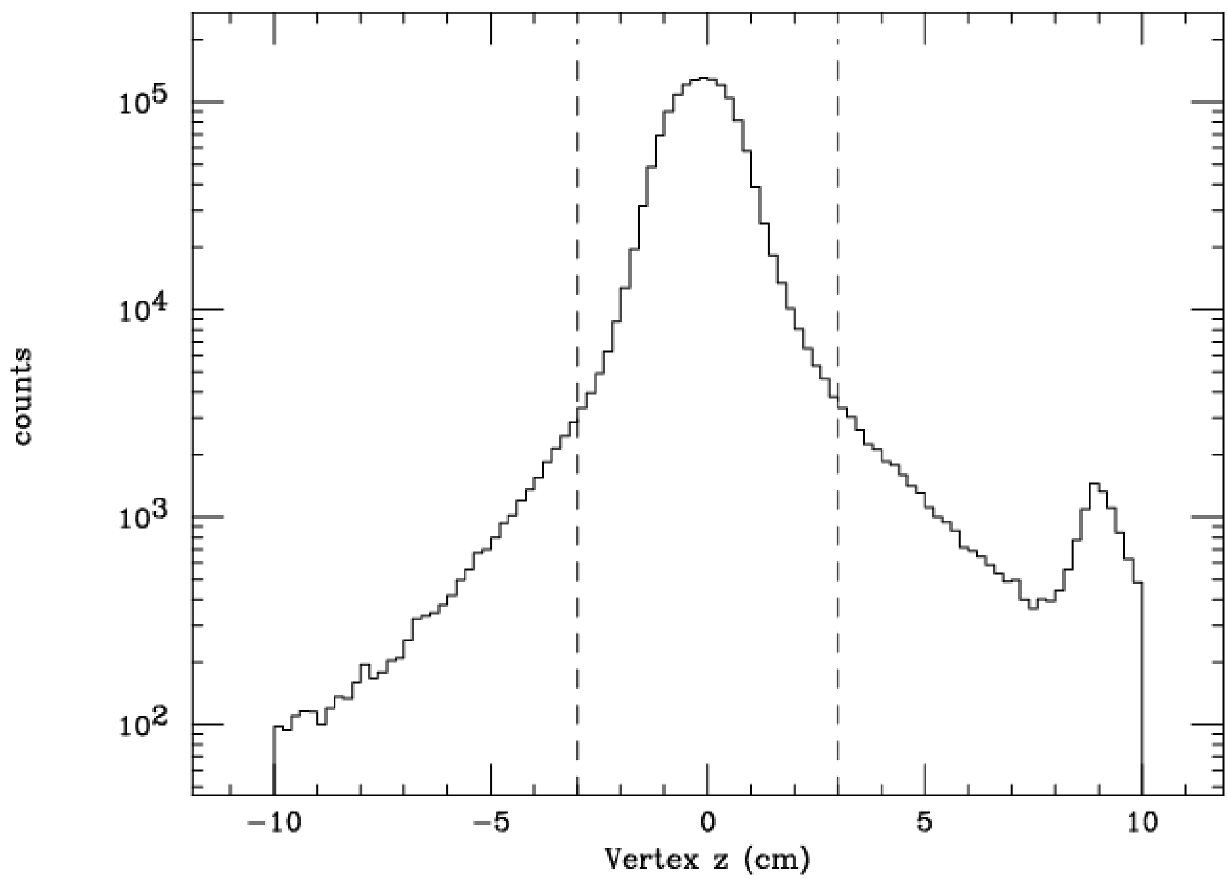

FIG. 4: Distribution of track vertex z (relative to nominal center of the target) for events with all other electron cuts applied. The vertical lines show the cut used in the analysis.

The new method uses the feature that the SC paddles and CC mirrors are close together so that their correlation is relatively insensitive to the track trajectories. The effectiveness of this cut is illustrated in Fig. 5.

- In order to remove random coincidences, the Cherenkov signal time must agree with the EC signal time within $\pm$ 4 nsec, as illustrated in Fig. 6. The distribution is asymmetric due to the fact that random hits are more likely to come before the good signal, but less likely to come after since the TDC has already been stopped by the good signals.

- The difference $\delta\phi_{DC1}$ between the electron's azimuthal angle at the first drift chamber layer and the azimuthal component of its momentum at the same location must be zero with $\pm 4^\circ$, as shown in Fig. 7. Particles with higher $\delta\phi_{DC1}$ are more likely to have scattered from materials that were not part of the target. Fig. 8 shows the z vertex

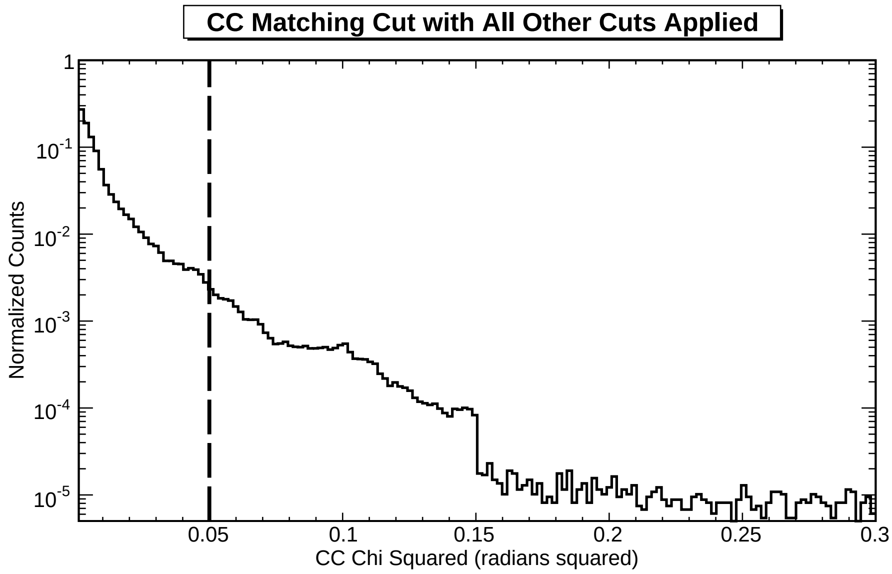

FIG. 5: Distribution of χ^2 for CC events with all other electron cuts applied. The vertical line shows the cut used in the analysis. The sharp drop-off at 0.15 is due to an early-stage software selection.

cut with and without the $\delta\phi_{DC1}$ cut. The log scale highlights several features that correspond to various target and beam-line vacuum windows and foils (see Ref. [50]).

- The electron scattering angle θ_e must be less than 40 degrees for Part A, and less than 45 degrees for parts B and C. Particles at larger angles could pass through the significant amounts of heat shields and super-insulation in the target. The increased radiation length of these materials resulted in high pair-symmetric backgrounds.

- Electrons whose trajectories passed too close to the lead shielding around the IC (or the IC support stand) were removed (see Ref. [19]). The looser of the two cuts described in this reference was used. Since the IC was octagonal in structure and has a thick support plate obscuring sectors 5 and 6, while CLAS is hexagonal, the cut depended on azimuthal angle, but was roughly 20 degrees (16 degrees) for Part A (parts B and C) for electrons originating at the target center. The cut eliminates electrons that pass through short lengths of the shielding, but survive, with strongly modified angles and momenta from multiple scattering and Bremsstrahlung. Most of these events have already been removed by the vertex and $\delta\phi_{DC1}$ cuts.

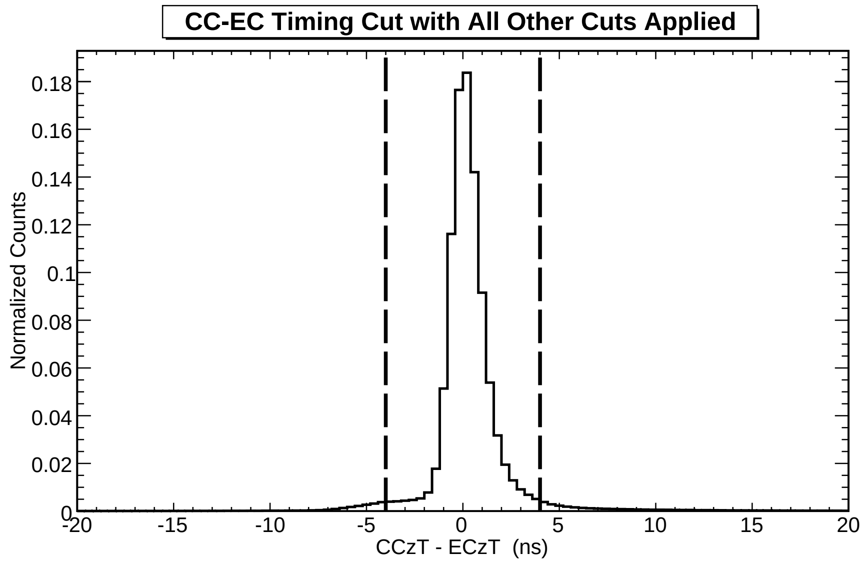

FIG. 6: Distribution of the time difference between CC and EC signals for events with all other electron cuts applied. The vertical lines show the cut used in the analysis.

E. Quality checks

1. Beam scraping

Thanks to careful on-line monitoring, very few data were taken with the beam scraping on the relatively thick and unpolarized target side walls. An off-line check revealed a few files with this problem [28], and they were removed from further analysis.

2. Rate stability

In order to avoid significant corrections to measured asymmetries (target single spin asymmetries, in particular), and also to obtain reliable dilution factors from the comparison of ammonia and carbon target rates, we removed data files where an obvious drop in efficiency occurred (see Ref. [29]). The most common reason was that the DC tripped off. The next most common reason was that the EC tripped off. Other problems were associated with the beam quality. In two cases, the Wein filter (which controls the beam helicity direction) was reversed in the middle of a run: these runs were removed. Some files were also removed due to low target polarization. In total, less than 5% of the data were discarded for one reason or another.

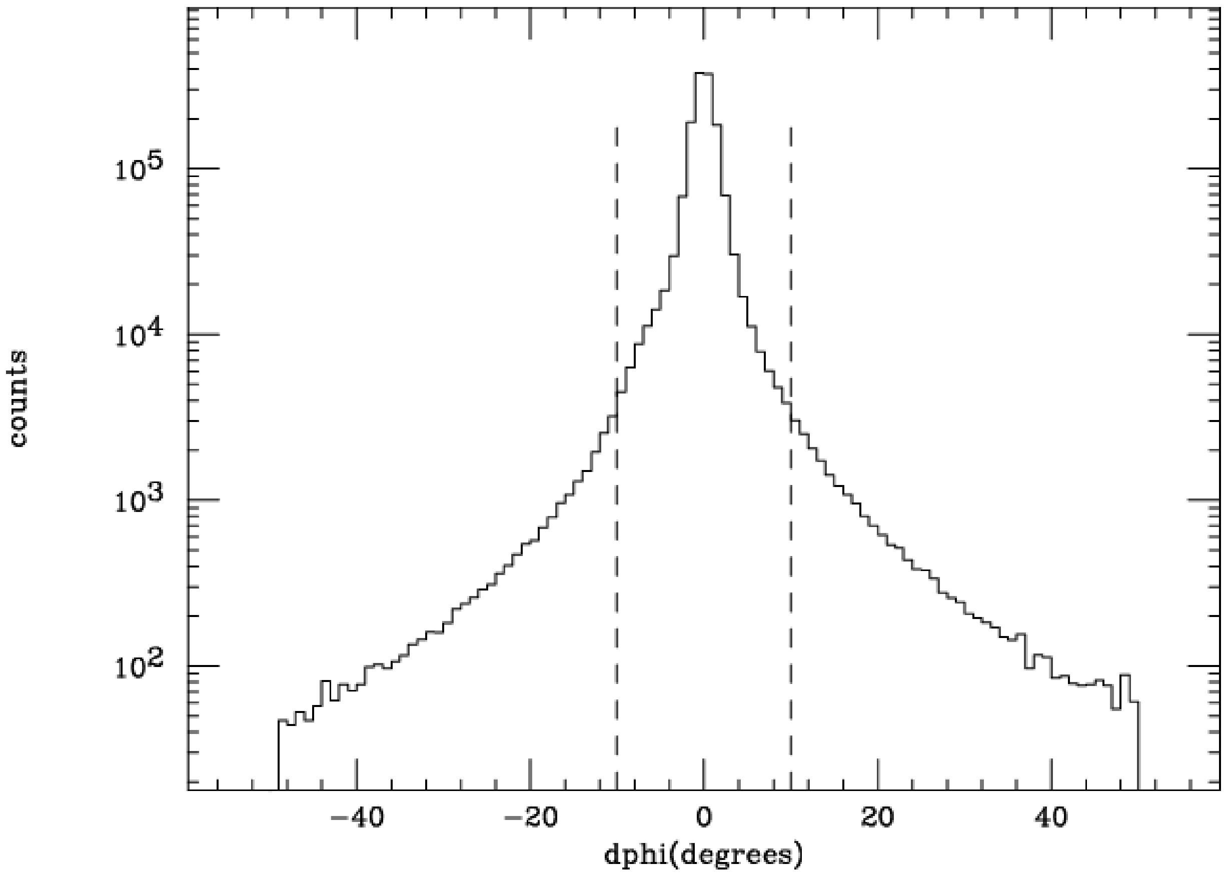

FIG. 7: Distribution of $\delta\phi_{DC1}$ with all other cuts applied. The vertical lines show the cut values used in the analysis.

The stability of the inclusive electron rates is illustrated in Fig. 9. The rates have been corrected for the luminosity-dependence discussed in Section IV B 8, as well as for the raster position correction for the ND_3 runs. The rates for NH_3 (blue and red points for top and bottom targets) are generally stable within one percent for several days. Over weeks to months,, there are slow drifts, possibly corresponding to changes in effective target thickness or overall detection efficiency. For Part B, these slow drifts are also seen for the carbon target runs interspersed throughout the data set. The 6% difference in target thickness between top and bottom cells in Part B is easily seen. The stability of the carbon runs (black points) is quite good in Parts B and C, but less so for the Part A, for which the rates have a total spread of about 7%. The reason for this instability was not found despite a fairly exhaustive search.

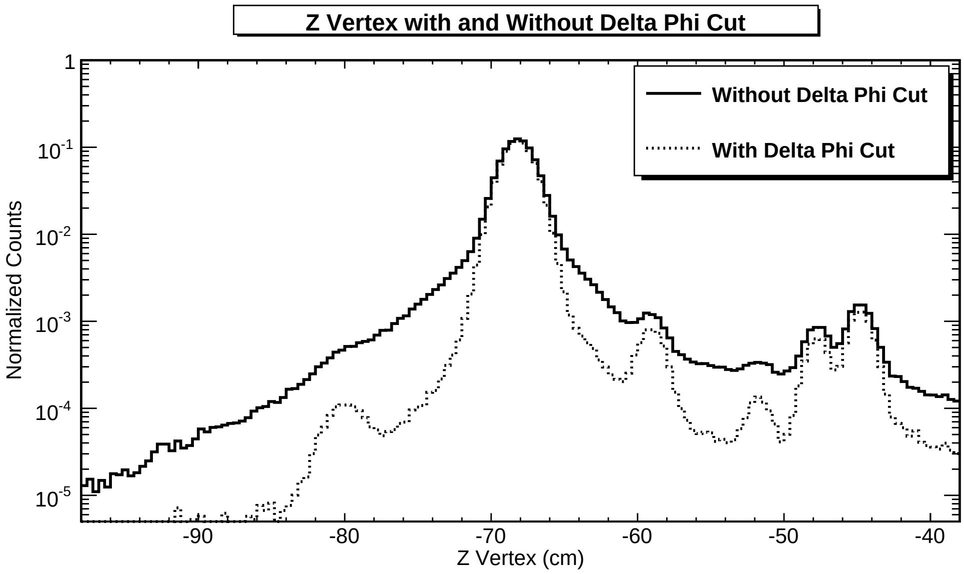

FIG. 8: The z vertex distribution plotted on log scale. The distribution is shown both with (dashed curve) and without (solid curve) the $\delta\phi_{DC1}$ cut.

3. Asymmetry stability

The average inclusive electron double-spin asymmetry proved to be a second very valuable quality check. Since the rates for ND_3 and carbon targets were very similar in part C, the inclusive rates alone could not distinguish a wrong target type in the run data base (which happened for about ten runs). The double-spin asymmetry is essentially zero for carbon targets, and generally at least 3-sigma different from zero for polarized targets. The sign of the asymmetry also checked that the overall beam and target polarized signs were correct in the data base. Several mistakes were found, for example when the beam half-wave plate was changed at a different time than initially recorded. Finally, this check was used to remove two runs where the half-wave plate was changed in the middle of a data run, and several runs where the target polarization suddenly dropped to zero due to target problems. Figure 10 shows the final results for the double spin asymmetry as a function of run number. In Part C, the NH_3 and ND_3 targets could also be distinguished due to the much smaller asymmetries for ND_3 compared to NH_3. After the fixes, the polarized target runs all show a positive asymmetry, while the carbon runs are all consistent with zero, as illustrated in Fig. 10.

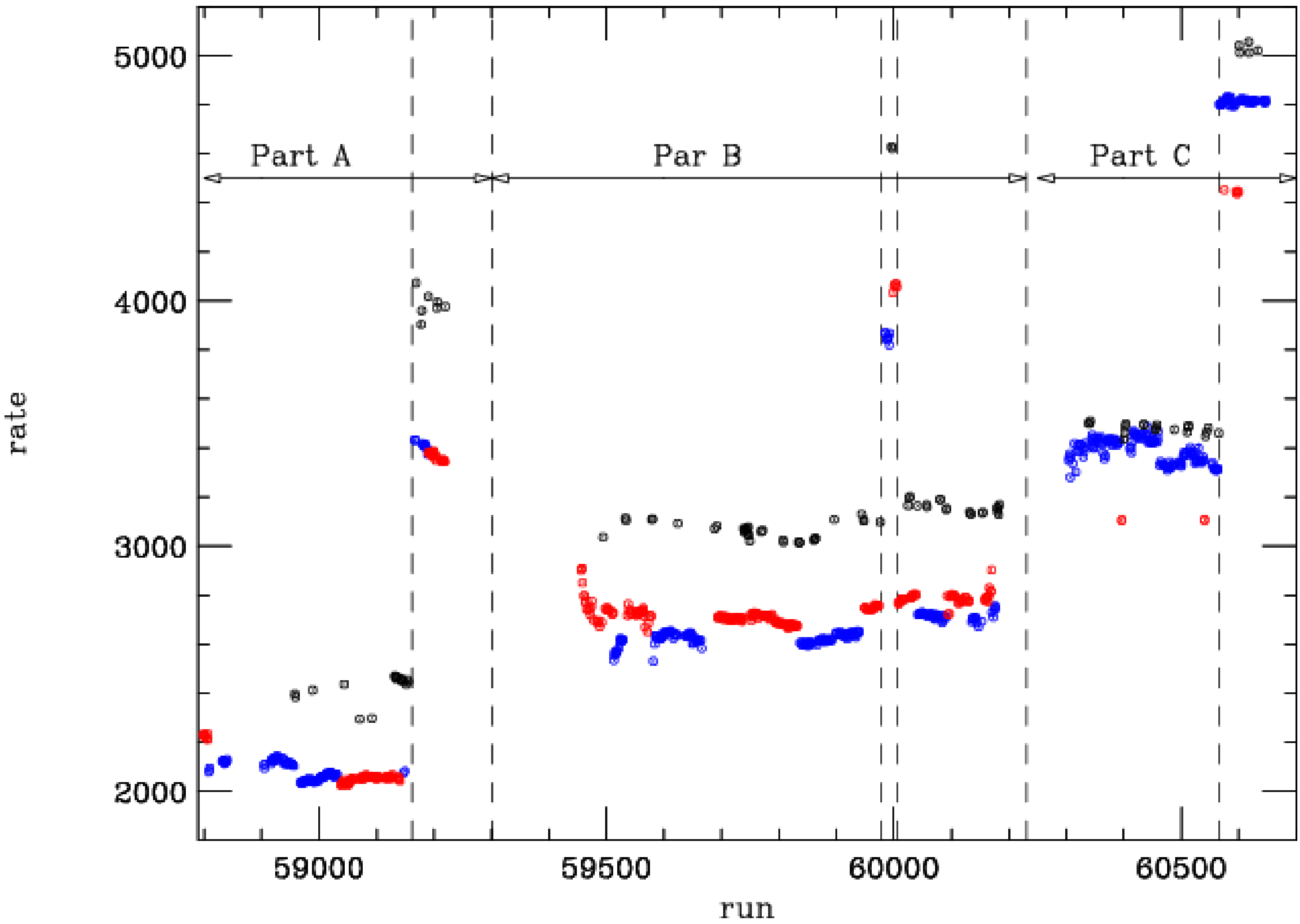

FIG. 9: Rates of inclusive electrons, normalized by incident beam charge, as a function of run number. Note that the vertical scale is offset from zero. The black points are for carbon, the red points for the bottom NH_3 targets, and blue points for the top NH_3 target (parts A and B) or the ND_3 target (Part C). The vertical dashed lines correspond to changes in beam energy or torus polarity.

4. Electron detection efficiency

Although the electron detection efficiency cancels in the double-spin asymmetries used to determine g_1, it must be reasonably high to obtain the smallest possible statistical error bars. The efficiency was determined by comparing the rates from the carbon target to those expected from a model of inclusive radiated cross sections [23] for the target materials present. Only events within $\pm 7^\circ$ in azimuthal angle of the center of each sector were used, to

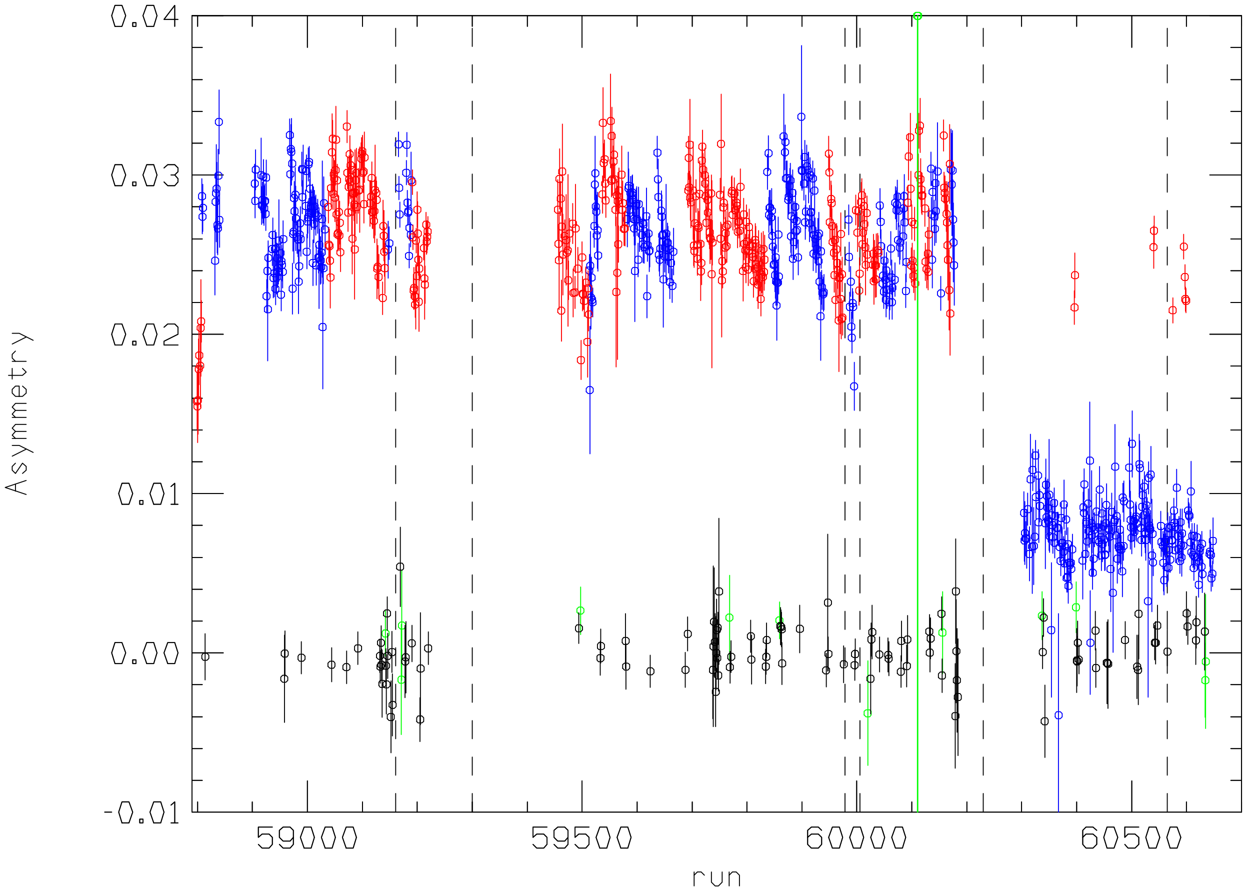

FIG. 10: Average raw double-spin asymmetry as a function of run number. The color scheme is the same as in 9, except that the green points are from the empty target which are below the scale in Fig. 9.

ensure that the acceptance would not be blocked by the torus coils. A correction to the data was made for contributions from pair-symmetric contributions. As illustrated in Fig. 11, the results show efficiencies between 70% and 95% over most of the kinematic range of the experiment. Regions where there are dead wires in the drift chambers are clearly visible. The very low gas Cherenkov detector efficiency for Sector 5 for most of the experiment (parts B and C) is also apparent. This problem was caused by a large leak, such that the gas medium was effectively air instead of the desired C4F10 (see Ref. [26]).

This purpose of this study was not to obtain precise efficiency information, but rather just to make sure that the system was behaving more or less as expected. For this reason, no attempt was made to study the detailed ϕ-dependence of the efficiency. The study proved very valuable in the initial running stage, where it was discovered that a wrong tracking parameter was resulting in very low (about 10%) track reconstruction efficiency. It was also useful in revealing leaks in the Cherenkov gas systems.

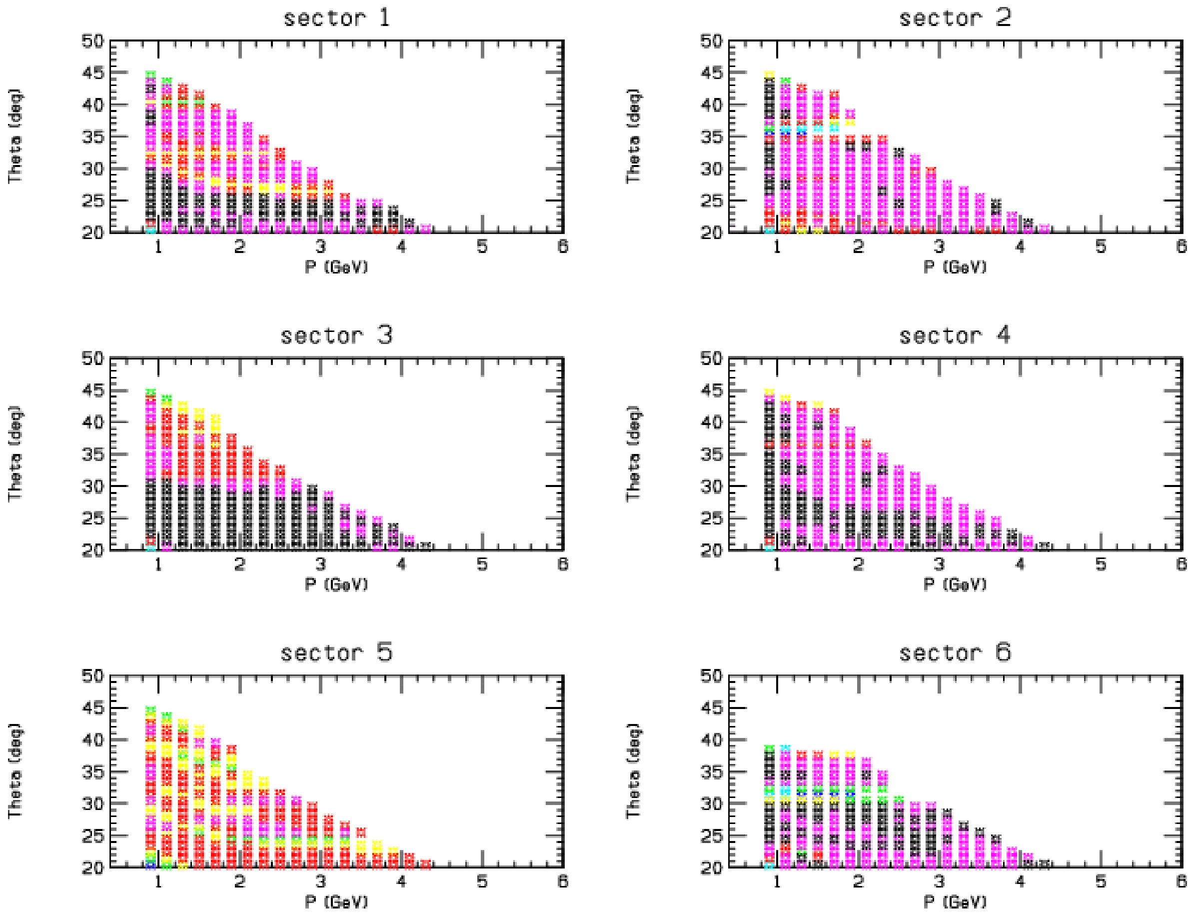

FIG. 11: Electron detection efficiency as a function of electron momentum P and azimuthal scattering angle θ for each sector using the 5.9 GeV beam energy runs of Part B. The color scheme, from lowest to highest efficiency in the interval 0 to 1, corresponds to blue, cyan, green yellow, red, magenta, and black (i.e. black is 0.84 to 1.0).

5. *Ad-hoc momentum and angle corrections*

Another quality check was to determine if any ad-hoc momentum or angle corrections were needed. Perhaps due to the careful DC alignment done for this experiment using both surveying and straight-through tracks [11], combined with the improved tracking through the target and torus magnetic fields mentioned above [16], no significant improvements could be made using ad-hoc corrections. This was determined by looking for deviations from the known neutron mass for the missing mass in the reaction $ep \to e\pi^+(n)$. For this study, a neutron was required to be detected within a few degrees of the predicted angle to reduce backgrounds (see Ref. [30]).

6. *Beam energy*

It is important to know the incident beam energy E_0 as well as possible, because this quantity is used for Q^2, x, as well as the depolarization factor, D.

The primary method was based on ep elastic scattering, using the relation

$$E_0 = M\{[\tan(\theta_e/2)\tan(\theta_p)]^{-1} - 1\}$$

where θ_e and θ_p are the electron and proton polar angles with respect to the beam line, and M is the proton mass. This method agreed with accurate measurements made in Hall A and Hall C, within 10 MeV. The results are $E_0 = 5.887$ GeV for Part A (beginning), $E_0 = 4.730$ GeV for Part A (end), $E_0 = 5.954$ GeV for Part B, and $E_0 = 5.752$ GeV for Part C. The estimated error is 10 MeV. These values correspond to the average value at the center of the target: the energy before entering the target is a few MeV higher due to ionization energy loss (see Ref. [27]).

III. PHYSICS ASYMMETRIES

A. Double-spin asymmetries

The double-spin asymmetry $A_\parallel$ was formed for each two-dimensional physics bin using:

$$A_\parallel = \frac{N_1 - N_2 r_c}{N_1 + N_2 r_c} \frac{c_s}{f\ (1 + c_1 + c_2)\ P_b\ P_t\ f_{RC}} + A_{RC} \qquad (2)$$

where N_1 (N_2) are the number of counts in the anti-parallel (parallel) beam helicity bins, r_c is the ratio of incident beam charges for the two helicity states, f is the bin-averaged dilution factor, defined as the ratio of events from polarized proton or deuterons in the NH_3 or ND_3 target to the total number of events, c_s is the pair-symmetric correction, c_1 accounts for polarized nitrogen in the NH_3 and ND_3 targets, c_2 accounts for the polarized NH_3 mixed into the ND_3 target, P_b is the beam polarization, P_t is the target polarization, f_{RC} is a 'radiative dilution factor', and A_{RC} is an additive radiative correction.

B. Raw asymmetry

The basic data processing consisted of determining the number of electron events passing the particle ID cuts mentioned above, for each run, in bins of momentum P, azimuthal scattering angle θ, and helicity (beam and target polarizations either aligned or anti-aligned). The main reason for choosing bins in (P, θ) at the data processing stage, was to allow flexibility later on to slightly vary the beam energy E_0 from the nominal value. Data were also binned in (W, θ) as a check.

The counts files were summed for each target and each of the following cases: Part A 5.9 GeV; Part A 4.7 GeV; Part B in-bending; Part B out-bending; Part C in-bending; and Part C out-bending. This is exactly the same procedure (i.e. summing counts over runs, and then forming an asymmetry) that was used to determine $P_b P_t$ (in which case there were not enough counts to form asymmetries on a run-by-run basis in each Q^2 bin followed by Gaussian averaging). A simulation showed that the small bias introduced by first summing counts, then forming asymmetries, is very well canceled if the same method is used for determining $P_b P_t$ and $A_\|$.

The bin sizes were 0.04 GeV in momentum and 0.2 degree in θ, chosen to be small enough to allow re-distribution into physics bins of (x, Q^2) and (W, Q^2), where W is the invariant mass of the final state:

$$W = \sqrt{M^2 + 2M\nu - Q^2} \tag{3}$$

Here, ν is the virtual photon energy, equal to the difference in the incident and scattered electron energies: $\nu = E - E'$, Q^2 is the four-momentum transfer:

$$Q^2 = -q^2 = 4EE' sin^2\frac{\theta}{2}, \tag{4}$$

and the Bjorken x is

$$x = \frac{Q^2}{2M\nu} \tag{5}$$

During the re-distribution process, the average values of all relevant physics quantities were calculated.

C. Charge asymmetry factor r_c

The ratio of incident beam charges takes into account any difference in the integrated incident current with one beam helicity compared to the other. Because the beam helicity was reversed at 30 Hz, and came in alternating helicity buckets, the difference came about only due to helicity-dependent beam current differences, which were kept less than 1 part in 1000 on a few minute time scale by a feedback system, and less than 1 part in 10000 averaged over a a month-long time scale. Thus effectively $r_c = 1$.

D. Dilution factor f

The dilution factor, f, is defined as the fraction of inclusive scattering events originating from polarized hydrogen or deuterium. The electron beam in our experiment passed through the following materials: helium (He), Kapton (K), ammonia ($^{14}NH_3/^{14}ND_3$), and aluminum (Al). The description of the target materials in the beam line is provided in Ref. [9] and an overview of the three target configurations is shown in Figure 12.

If we define $n_{material}$ as the electron scattering rate from a particular target material, we can write, *e.g.* for the proton:

$$f = \frac{n_{proton}}{n_{NH_3} + n_{He} + n_{Al} + n_K}. \tag{6}$$

The event rate for each material i is proportional to the product of the areal density $\tilde{\rho}$ and inclusive DIS cross section σ:

$$n_i \propto \tilde{\rho}_i \sigma_i = \rho_i l_i \sigma_i, \tag{7}$$

where ρ_i is the volume density and l_i is the length of the each material. The constant of proportionality depends on detector acceptance and very slightly on z-vertex position, but since all the materials are in the same target configuration, the constant is the same for

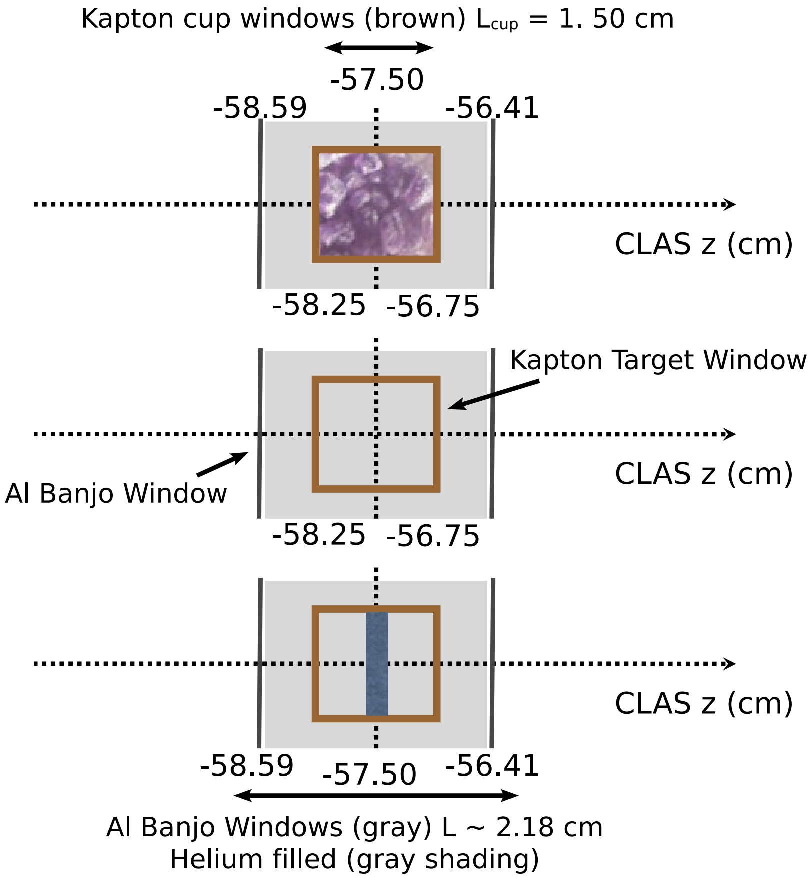

FIG. 12: Overview of the targets used: loosely packed ammonia beads, an empty target cell, and a solid carbon target. Ammonia was the primary experimental target used; carbon and empty targets were used to calculate dilution factors and for consistency checks.

the numerator and denominator. Using the symbol A for $^{14}NH_3$, We can now rewrite the dilution factor in terms of these quantities mentioned above as

$$\frac{\frac{3}{17}\rho_A l_A \sigma_A}{\rho_{He}(L - l_A)\sigma_{He} + (\frac{14}{17}\sigma_N + \frac{3}{17}\sigma_p)\rho_A l_A + \rho_{Al} l_{Al}\sigma_{Al} + \rho_K l_K \sigma_K} \tag{8}$$

The radiated cross sections are a function of the length of the material in units of radiation length and are obtained by modeling the available world data (see Ref. [23]), and the areal density for each material was measured in the lab or obtained from literature. The necessary quantities are listed in Table II, below.

As shown by Eq. 8, to accurately determine the dilution factor we need to know the total length between banjo windows (L) in the target and the packing fraction or 'length' (l_A) of

Property	Helium	Carbon	Aluminum	Kapton	NH_3	ND_3
Volume Density ρ ($\frac{\mathrm{gm}}{\mathrm{cm}^3}$)	0.145	2.193	2.700	1.430	0.866	1.007
Radiation length X_0 ($\frac{\mathrm{gm}}{\mathrm{cm}^2}$)	94.26	42.66	24.03	40.54	40.80	50.93
Length (cm)	L, $L - l_A$, $L - l_C$	0.398	0.0166	0.0066	l_A	l_A
Molar Mass ($\frac{\mathrm{gm}}{\mathrm{mol}}$)	4	12	27	382	17	20
Mol of nucleons/cm^2	0.2725	0.7632	0.03969	0.009437	$1.3755\frac{l_A}{1.5}$	$1.584\frac{l_A}{1.5}$

TABLE II: Numbers used to calculate areal densities $\tilde{\rho}_i$. The total length of the target cup was 1.5 cm which is used in the last two rows.

the NH_3 beads in the target cup.

1. Length between banjo windows (L)

The distance L between the aluminum banjo windows (illustrated in Fig. 12) was measured at room temperature to be 2.3 ± 0.3 cm. Another large uncertainty also arises because the windows are very thin and and hence can bow inwards or outwards, depending on pressure differences.

We therefore relied primarily on data taken with the empty target and no helium bath. The two peaks in Fig. 13 are from the aluminum banjo windows, with the small inner shoulder coming from the much thinner Kapton foils. The peak separation from these measurements is 2.0 ± 0.1 cm. Unfortunately, the target group was not able to calculate reliably if the windows would bow inward or outward depending on target configuration (i.e. with or without helium in the bath). This uncertainty is taken into account in the systematic error (discussed below).

A check was made by extracting L from measurements of the empty and carbon targets, with and without helium present, assuming a helium density of 0.145 $\frac{mathrmg}{\mathrm{cm}^3}$. The average value of L from a set of 10 such measurements was 2.1 ± 0.1 cm.

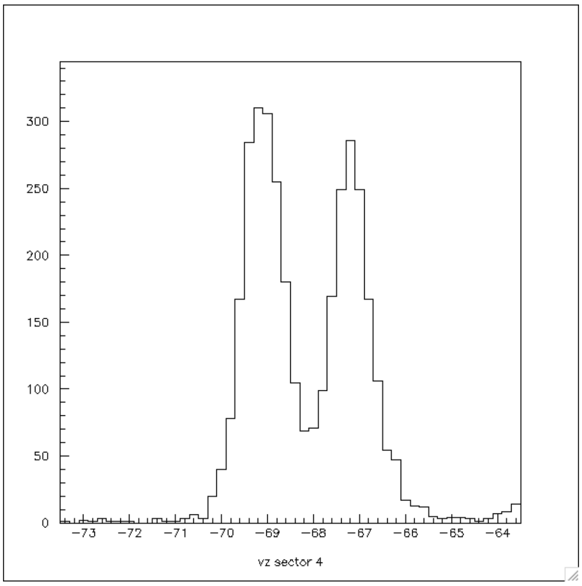

FIG. 13: Count rates as a function of vertex z (in cm) from an empty target run with no helium bath present. The quantity L was determined from the distance between these two peak positions.

2. *Ammonia length l_A (the packing fraction)*

The other quantity extracted is the packing fraction of the ammonia beads in the Kapton target cup. This gives us the apparent length of the ammonia target if it is all packed into a solid piece as opposed to crushed beads.

The method used to determine l_A was to fit the value that best described the measured ratios of electron rates from the carbon and ammonia targets. The value of l_A was varied, and for each value the predicted ratio of carbon to ammonia events was calculated in bins of W and Q^2. The predictions used look-up tables of radiated cross sections for the various possible target materials (p, d, He, C, N, and Al), based on a fits to world data [20–22]. Both internal and external radiative corrections were applied to the cross sections in the table. Since external corrections depend on the total target thickness, which in turn depends on l_A, the look-up tables included the radiative corrections for the highest and lowest possible values of l_A, and an interpolation was done to obtain predicted ratios of radiated cross sections at intermediate values of l_A. For each carbon target run, the run on ammonia closest in time was chosen to obtain a value of l_A in order to minimize the effects of slow drifts in average detection efficiency.

Figures 14 and 15 show the values obtained for parts (A,B) and part C, respectively.

Values are shown for all of the separate targets, including the Top and Bottom cups for Parts A, B and C. The errors on any individual measurement of l_A are minuscule, but there is a typical spread in results of about 0.02 cm for Parts A and B. We therefore assigned an error of 0.06 cm to the measurements of l_A. The spread for part C ND_3 target is larger, probably due to the "settling" that occurred in the target, and the subsequent sensitivity to beam position and average raster size. The systematic errors on l_A and dilution factor are discussed below.

A summary of the data is presented in Table III.

Run Range	Target Cup	L (cm)	l_A (cm)	l_A Error (cm)
Part A (58799 - 59300)	NH_3 Top	2.1	0.853	± 0.06
Part A (58799 - 59300)	NH_3 Bottom	2.1	0.851	± 0.06
Part B (59300 - 60185)	NH_3 Top	2.01	0.860	± 0.06
Part B (59300 - 60185)	NH_3 Bottom	2.01	0.910	± 0.06
Part C (60242 - 60645)	NH_3	2.05	0.922	± 0.06
Part C (60242 - 60645)	ND_3	2.05	0.890	± 0.06

TABLE III: A summary of target length and ammonia length data for all parts.

3. *Raster correction to effective length of ND_3*

At the beginning of Part C, the ND_3 target cell was packed full of beads. After the target accidentally received a dose of high peak-current "pulsed" beam when the operator was doing some beam tuning, the beads broke up into smaller pieces, and compacted down, leaving a several-mm-high gap with no beads near the top of the cell. To compensate, the raster pattern was changed from round to elliptical, and re-centered to minimize the amount of beam passing through liquid helium only. For some period of time, the centering drifted too high, and there was a loss of event rate. This is illustrated in Fig. 16, where the rate of good electrons is plotted versus the average vertical raster magnet ADC reading. The dashed line shows the correction function, given by Eq. 9, used to parametrize the effective decrease in target thickness as a function of average magnet current Y_r. This correction was only applied for $Y_r > 3800$ ADC counts.

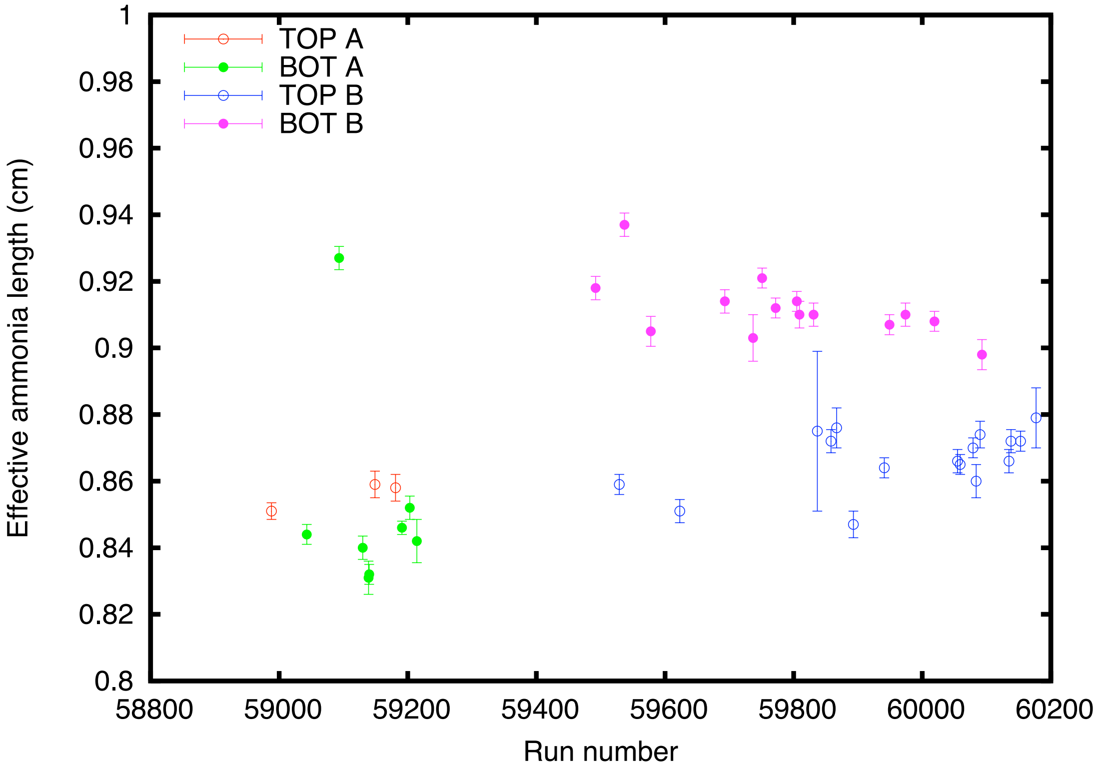

FIG. 14: Ammonia effective length l_A calculated over a range of runs from Parts A and B using different pairs of carbon and ammonia runs. Selections from both top and bottom cups from each part are shown.

$$Correction = 1 + \frac{140}{2150}\frac{(Y_r - 3800)}{400} \tag{9}$$

4. NH_3 contamination of ND_3 target

The manufacturer's specification for the deuterium gas used to make the ammonia beads had $< 1\%$ hydrogen contamination. A check was made using *ep* elastic data, and the actual contamination was, surprisingly, found to be an order of magnitude larger. After standard *ep* elastic exclusivity cuts, similar to those described in the next section, the events from

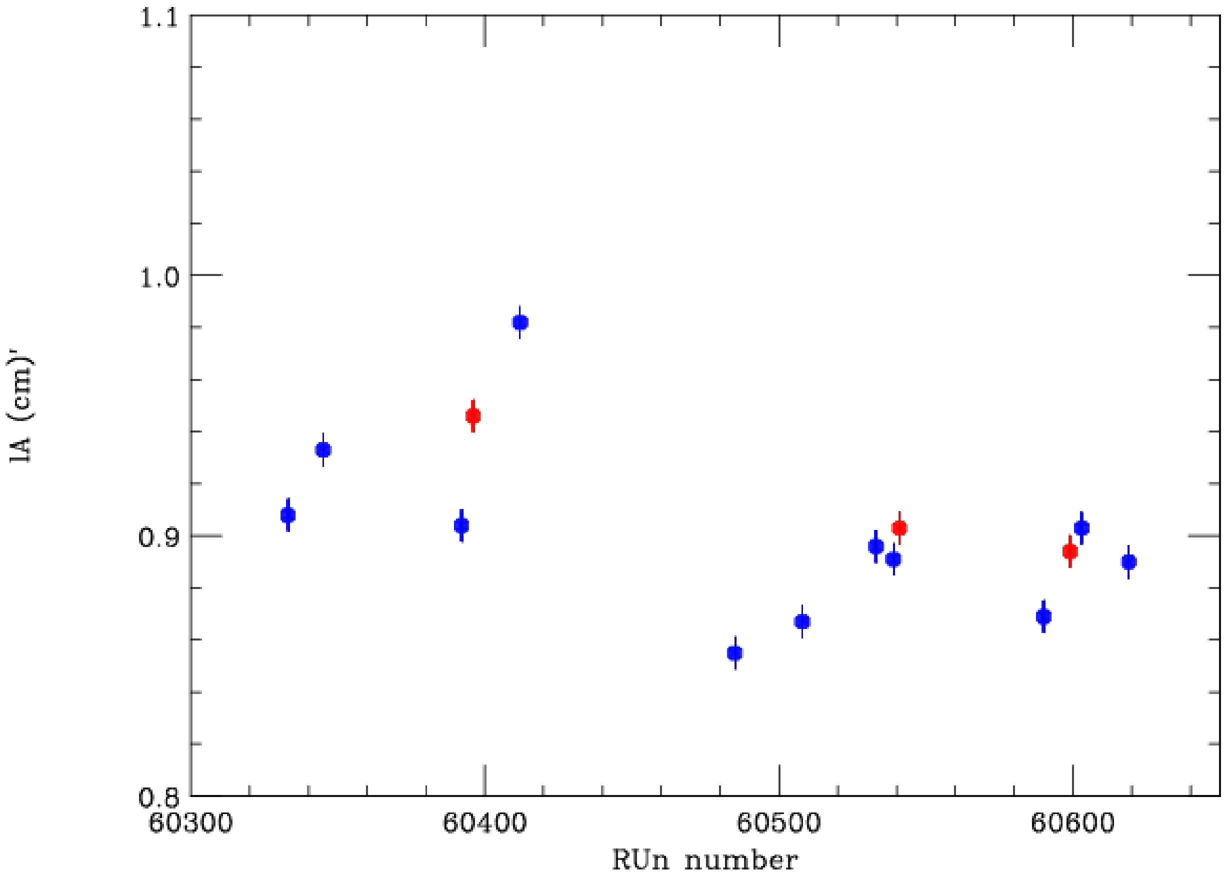

FIG. 15: Ammonia effective lengths l_A as a function of run number in Part C. Blue points are for ND_3, and red points are for NH_3.

hydrogen, deuterium, and heavier nuclei could clearly be distinguished by plotting the event rates as a function of missing transverse momentum. In the case of a free proton, the missing momentum distribution is a delta-function widened by our experimental resolution. In the case of the deuteron, it is considerably wider due to the average 50 MeV Fermi motion of a proton in a deuteron. In the case of heavier nuclei such as carbon and nitrogen, the peak is another factor of four wider, as the typical Fermi momentum is of order 200 MeV. These features are clearly illustrated in Figure 17. The distribution of missing momentum for the carbon target is very wide, and that for the NH_3 target has very narrow peak, sitting on top of a wide distribution with the same shape as the carbon target. The ND_3 target spectrum has the expected medium-width peak from free deuterons in the target, again sitting on top of a nuclear background from nitrogen. Unfortunately, a very narrow peak of the same width as seen in the NH_3 target is also clearly visible. Using data from the carbon and NH_3 targets as a guide, we performed fits to the three components visible in the ND_3

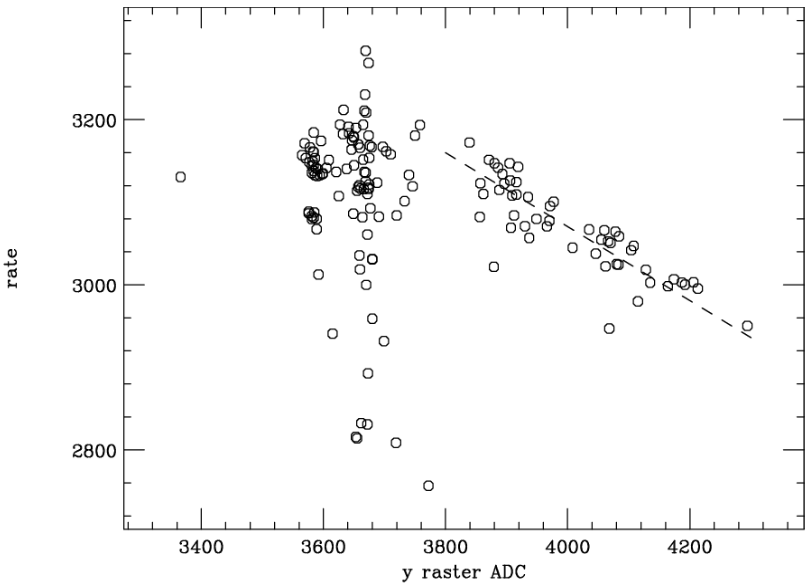

FIG. 16: Rate of detected electrons from the ND_3 target in Part C (in-bending runs only) as a function of the average vertical raster magnet reading.

spectra to obtain the relative fraction of free protons and deuterons. The result of the study was that $10.5 \pm 0.4\%$ of the ND_3 effective target length was NH_3, for the in-bending runs, and $12.0 \pm 0.7\%$ for the outbending runs. No time-dependence to the contamination was observed within each of these run periods. The study was performed independently by P. Bosted and S. Koirala, using different exclusivity cuts and fitting methods. The two results were in good agreement (see Refs. [24] and [25]).

As a further check, a direct measurement was made on a portion of the ND_3 beads from Part C using an NMR technique. This technique involved creating a water-based ammonia solution that was doped with a known amount of a hydrogen-bearing molecule. Then the relative heights of the NMR peaks could be compared and the hydrogen contamination measured. Although the errors from this method turned out to be too large to draw a firm conclusion, the results implied that the contamination was more likely to be on the order of 10% than 1%.

5. *Dilution factor results*

Having determined the areal density of each component of each target, we used the method outlined above to calculate the corresponding dilution factor as a function of (x, Q^2)

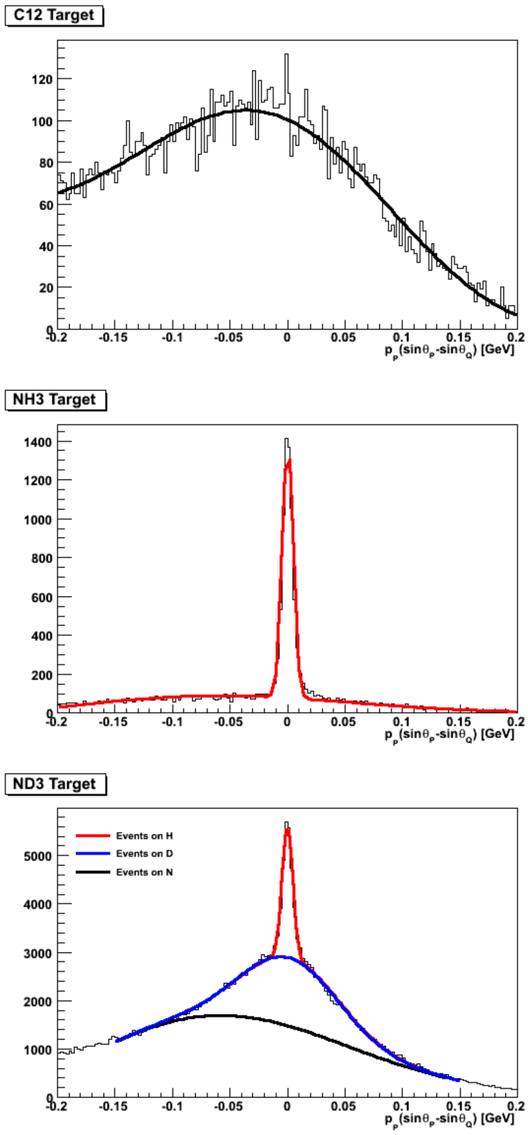

FIG. 17: Spectra of exclusive electron-proton coincidences plotted versus the transverse component of missing momentum, for a carbon target run (top), a NH_3 target run (middle), and a ND_3 target run (bottom). The red, blue, and black curves in the bottom panel show the contributions from free protons, protons bound in deuterium, and protons bound in heavier nuclei, respectively.

and (W, Q^2). The results for the Top NH_3 target in Part A are shown in Fig. 18. The gradual increase with x is due to the roughly $(1 - 0.8x)$ behavior of the neutron-to-proton inclusive cross section ratio. The oscillations at $W < 2$ GeV are due to resonance structure, which is washed out in $A > 1$ nuclei compared to the free proton.

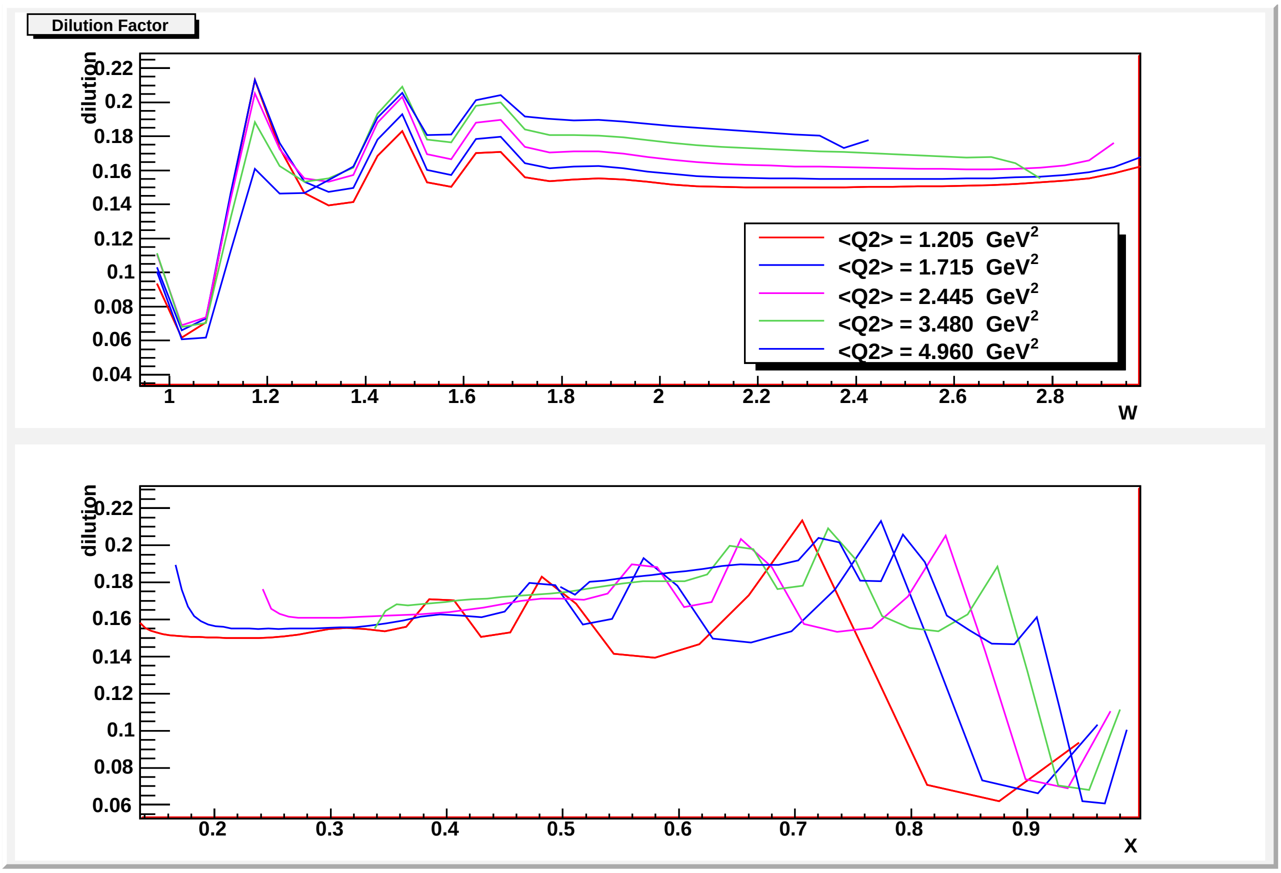

FIG. 18: Dilution factor for the proton target as a function of W (GeV) in top panel, and as a function of x in the bottom panel, for selected values of Q^2.

E. Target and beam polarization

For this inclusive analysis, only the product of target polarization (P_t) and beam polarization (P_b) is important. As explained below (see section on systematic errors), there is a very small contribution from parity-violating electron scattering that depends only on beam polarization, which can be canceled out by running for equal times with positive and negative target polarization.

For the NH_3 targets, the individual measurements of each quantity (NMR for P_t, Møller scattering for P_b) had relative systematic errors of over 5%. We therefore used ep elastic scattering, for which the error on the measured asymmetry is of order 1% statistical, and $< 2\%$ systematic. Another advantage is that the same runs were used as for the inclusive analysis, so any run-dependent biases would tend to cancel.

We selected electrons using particle ID cuts similar to those used for the inclusive analysis.

We selected protons using a ± 0.7 nsec cut on the difference in predicted and measured times between the electron and proton, determined with the SC system. The cuts used to select ep elastic events were:

- missing energy less than 120 MeV
- missing longitudinal momentum less than 120 MeV
- missing transverse momentum less than 80 MeV
- $|W - M| < 0.08$ GeV
- beam energy reconstructed from electron and proton polar angles within 70 MeV of the nominal value.

The last cut was especially powerful in reducing the background from quasi-elastic events from nitrogen to about 3%. This was determined by scaling the rates from the carbon target by the ratio of integrated beam currents, as well as the ratio of effective target thicknesses for materials with $A > 1$. The scaled rates were found to match very well outside the E_0 cut region. Events in each Q^2 and helicity bin were summed over all runs with similar rates. We only used two helicity bins, corresponding to beam and target polarizations aligned or anti-aligned. The top and bottom target cups were not separated in this analysis. The dilution-corrected double-spin asymmetry was then formed for each Q^2 bin, and P_bP_t was extracted as the ratio to the expected asymmetry. The values were then averaged over Q^2, which ranged from about 2 to 7 GeV^2. No dependence on Q^2 was observed. The results are given for each set of running conditions in Table IV.

In the one-photon exchange approximation, the predicted asymmetries only depend on one quantity, which is the ratio of proton electric to magnetic elastic form factors G_M/G_E. We used a simple fit to the results of the polarization transfer experiments [31], which is $G_M/G_E = \mu_p/(1 - Q^2/9)$, where Q^2 is in units of GeV^2, and $\mu_p = 2.79$. As a check, we also tried $G_M/G_E = \mu_p$, which is the result from the Rosenbluth fit experiments [32], which have large two-photon corrections, not applicable to our situation. Nonetheless, at our beam energy of 6 GeV, it makes only $\sim 1.4\%$ difference in the averaged P_bP_t results, as seen in Table IV. In the three high-statistics cases, the χ^2/d.f. for the average over Q^2 is slightly larger, but since the values of χ^2/d.f. are less than unity in both cases, the change in likelihood" is not significant, and both can be regarded as equally good fits.

	$G_M/G_E = \mu_p/(1 - Q^2/9)$		$G_M/G_E = \mu_p$	
Case	P_bP_t	χ^2/d.f.	P_bP_t	χ^2/d.f.
Part A (5.9 GeV)	0.637 ± 0.011	0.491	0.628 ± 0.010	0.547
Part A (4.8 GeV)	0.652 ± 0.011	1.057	0.648 ± 0.011	1.199
Part B (in-bending)	0.645 ± 0.007	0.891	0.637 ± 0.007	1.009
Part B (out-bending)	0.579 ± 0.037	0.962	0.572 ± 0.036	0.951
Part C (in-bending)	0.50 ± 0.04	x	x	x
Part C (out-bending)	0.51 ± 0.06	x	x	x

TABLE IV: Average values of proton P_bP_t for parts A and B, for two choices of the ratio of proton magnetic to electric form factors. The results using $G_M/G_E = \mu_p/(1 - Q^2/9)$ were those used in extracting the spin structure functions. The values of χ^2 are for the averaging over Q^2. The results for Part C are for the 10.5% of NH_3 contaminating the ND_3 target.

The sensitivity to cuts was checked by using both a wider and a tighter set. The results were consistent, within the expected errors.

For the ND_3 target, the kinematic region where there is the best sensitivity to *ep* quasi-elastic scattering was heavily contaminated by the polarization of the 10% NH_3 in the target. On the other hand, the direct deuteron polarization measurements using NMR are more accurate than for the proton, thanks to the "double peak" fitting method, which removes the sensitivity to the hard-to-measure thermal equilibrium signal (see Ref. [33]).

We therefore used the count-weighted product of target polarization from NMR and beam polarization from Møller measurements to obtain:

- Part C in-bending runs: deuteron $P_bP_t = 0.216 \pm 0.010$
- Part C out-bending runs: deuteron $P_bP_t = 0.236 \pm 0.010$

The error is based on an estimated systematic error of 3% in P_t and 4% in P_b. Using these values as a constraint, we then fit the *ep* coincidence data in the region of small missing momentum, to obtain $P_bP_t = 0.50$ for the protons in the ND_3 target [24].

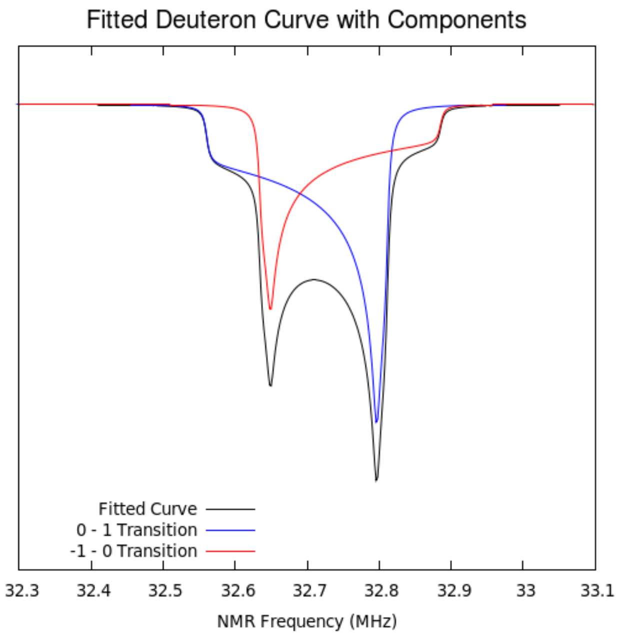

FIG. 19: A deuteron NMR frequency sweep spectrum showing peaks from both transitions as well as their sum. The relative heights of the two peaks is related to the deuteron polarization.

1. *Deuteron polarization*

The polarization of the deuteron target is determined using an NMR system which measures the magnetic susceptibility of the material. The output curve from this system is proportional to the polarization of the material but the constant of proportionality is not well known. To find this constant, the area of the signal when the target is at thermal equilibrium (TE) is compared to the polarization calculated using statistical mechanics. For deuteron targets, however, the TE signal is so small that the error is increased substantially compared to the proton target. An alternate method, described next, exploits the spin-1 nature of the deuteron.

As shown in Figure 19, the deuteron NMR curve is a superposition of curves. The spin-1 system of the proton and neutron is split into three states, and the two equally sized transitions are stimulated equally by the NMR. Thus, whichever state is more highly populated yields a larger curve. By fitting this curve with an equation derived from the physics of the deuteron [49] and comparing the ratio of these components it is possible to calculate the polarization. Due to the complexity of the fitting function, getting reliable polarization measurements for every run proved impossible; therefore, a hybrid method was developed. For multiple runs where the function fits exceptionally well (generally polarization values above 30%), spread throughout the run period, the polarization was compared to the area of the curve and a calibration constant calculated. These calibration constants were then used in lieu of the calibration constants derived from TE measurements. For more details see [33].

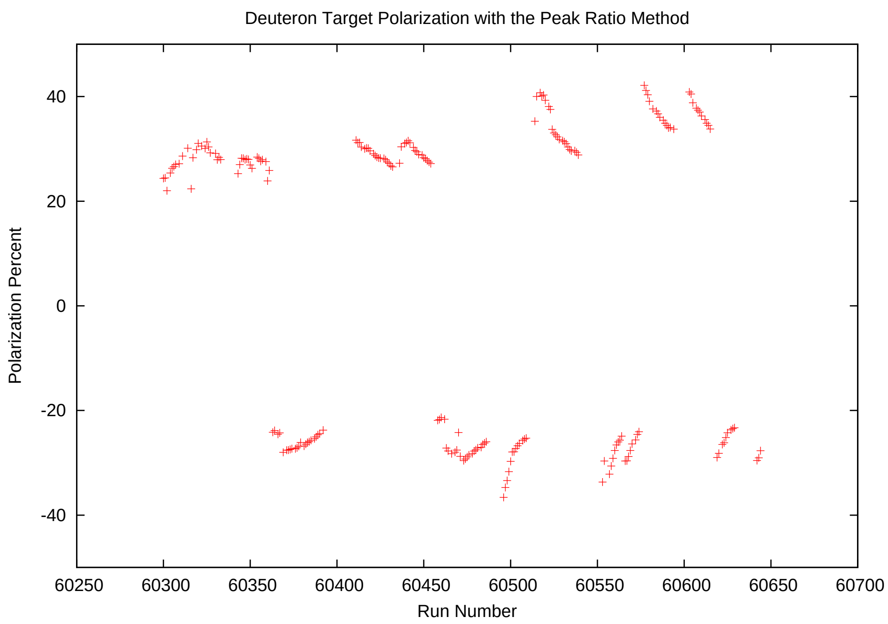

FIG. 20: Run-averaged target polarizations are shown for the deuteron runs in Part C.

F. Pion and pair-symmetric correction

Another correction to the asymmetry comes from the inclusion of negative pions and electrons produced in pair-production processes. The correction for this contamination is of the form:

$$A_{corr} = A_{raw}\frac{1-\sum_i R_i A_i/A_{raw}}{1-\sum_i R_i} \tag{10}$$

where R_i is the ratio of rates for a particular process to the electron rate and A_i is the asymmetry for the process [48].

Dalitz decay of the π^0 ($\pi^0 \to \gamma e^+ e^-$) or Bethe-Heitler conversions of one of the photons from "normal" π^0 decay ($\pi^0 \to \gamma\gamma$) will both produce electron-positron pairs. Since there are equal numbers of electrons and positrons produced from π^0 decays, the rate and asymmetry of positrons can be used to correct the electron sample. Due to the fact that electrons and positrons bend in opposite directions in the toroidal field (and thus have different acceptance), we cannot directly use the electron and positron rates for a given torus polarity. Fortunately, we took a considerable amount of data with opposite torus fields, to compare the electron/positron rates with both particles in-bending or both particles out-bending. About 50 runs from each of the in-bending and out-bending sections of Part C were analyzed with the standard electron cuts applied equally to the electron and positron samples. The results, binned in momentum and polar angle (p, θ), are shown in Figure 21, for the case where both electron and positron are in-bending (red), and where both are out-bending (green).

The ratios of e^+/e^- are compared with two predictions in Fig. 21. The black curves are the predicted ratios assuming that all the positive particles are actually positrons and not mis-identified pions. As discussed in Ref. [48], the only significant source of positrons for $\theta > 16$ degrees and a beam energy of 6 GeV is from π^0 decays. This includes both the Dalitz decay into $\gamma e^+/e^-$ which has a branching ratio of 1.2%, and the normal decay to $\gamma\gamma$ where one of the photons converts to $e^+/e-$ in the field of one of the nuclei in the target, target windows, air between the windows and the first drift chamber (DC1), or in DC1 itself. The cross section for inclusive π^0 yields was taken as the average of yields for π^+ and π^-, measured at both 5 and 7 GeV electron beams at SLAC [47]. A simple Monte-Carlo generator taking into account our target configuration performed the π^0 generation and decays and calculated the cross sections in bins of spectrometer P and θ. These were divided by the well-known inclusive electron cross section to obtain the ratios shown as the black curves. Good agreement is found in both shape and magnitude up to about 2.6 GeV, considering the approximately 30% uncertainty in the calculation.

The clear excess above 2.6 GeV can be attributed to detected π^+ passing the positron selection criteria. The expected rate, shown as the blue curves in Fig. 21, was modeled using the fit to SLAC data mentioned above to calculate the pion cross sections. The pion rate was reduced everywhere by a factor of ten to simulate the approximate rejection power

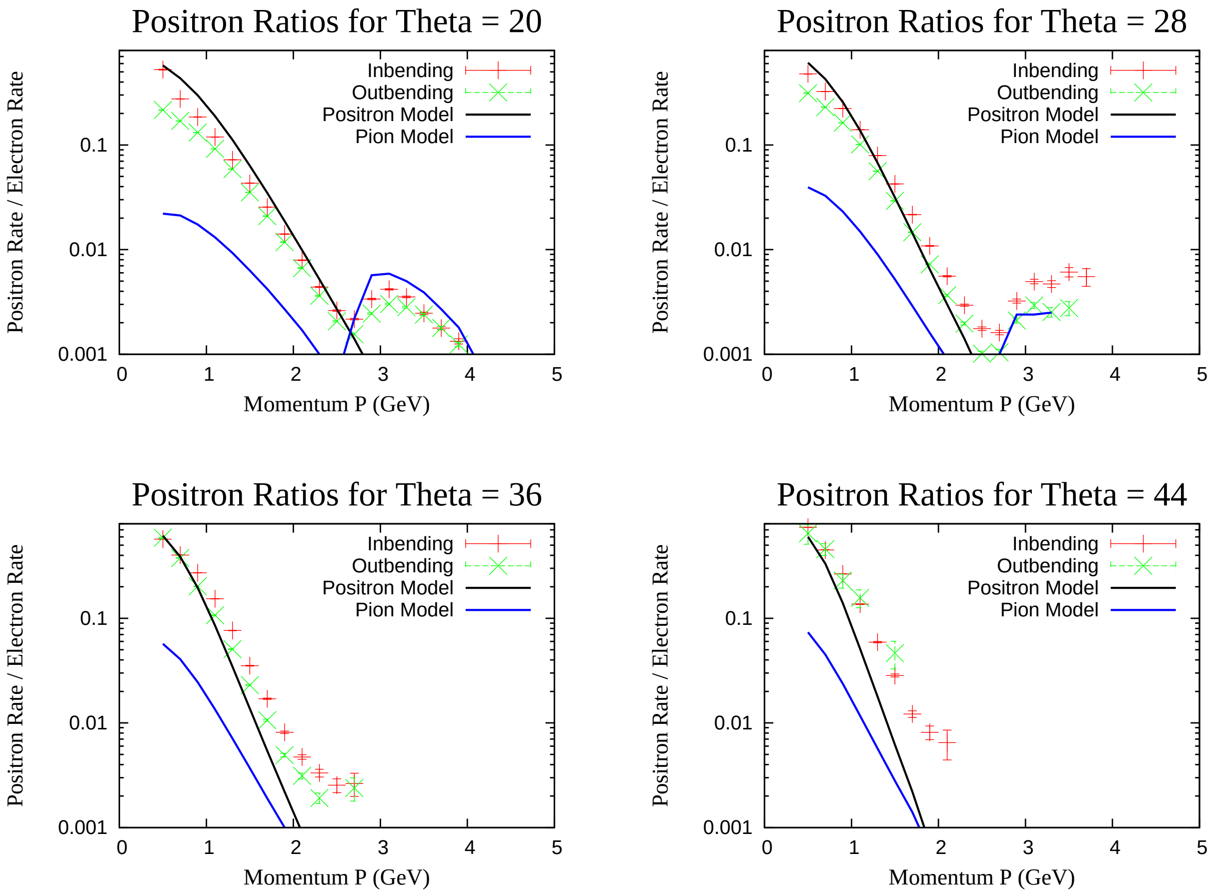

FIG. 21: Ratio of positron to electron inclusive rates as a function of momentum, for four bins in polar scattering angle θ. The green points are both particles out-bending in the torus, and the red points are both particles in-bending. The curves are explained in the text.

of the E/P cut. The Cherenkov detection efficiency (relative to that of an electron) was considered as 100% above 3.6 GeV, dropping to only 1% at the pion threshold of 2.65 GeV. The 1% value stems from a rough estimate of the pion colliding with an atomic electron in the Cherenkov window or gas medium and the "knocked-out" electron being well above the few-MeV-threshold to emit Cherenkov radiation. The simulation accounts quite well for the enhancement seen above 2.65 GeV, and also strongly suggests that positrons dominate over pions at lower momenta. The largest pion to electron ratio is only about 0.3% (near $P = 3$ GeV). We make the pion contamination correction assuming that negative and positive pion yields are identical. The measurements of Wiser [47] show up to 30% difference in π^+ and π^- yields, which we did not take into account, because the net effect is negligible with the small pion contamination of this analysis.

The other factor in determining the correction is the ratio of the asymmetries, scaled by the ratio of rates (i.e. $\frac{e^+_{rate}/e^-_{rate}}{e^+_{asym}/e^-_{asym}}$). Figure 22 shows that the positron (and mis-identified pion) asymmetry contribution is consistent with zero on average, for both deuteron and proton targets. There is some indication of significant contributions for $P < 1.2$ GeV, but these are removed by the $y < 0.8$ cut used in the analysis.

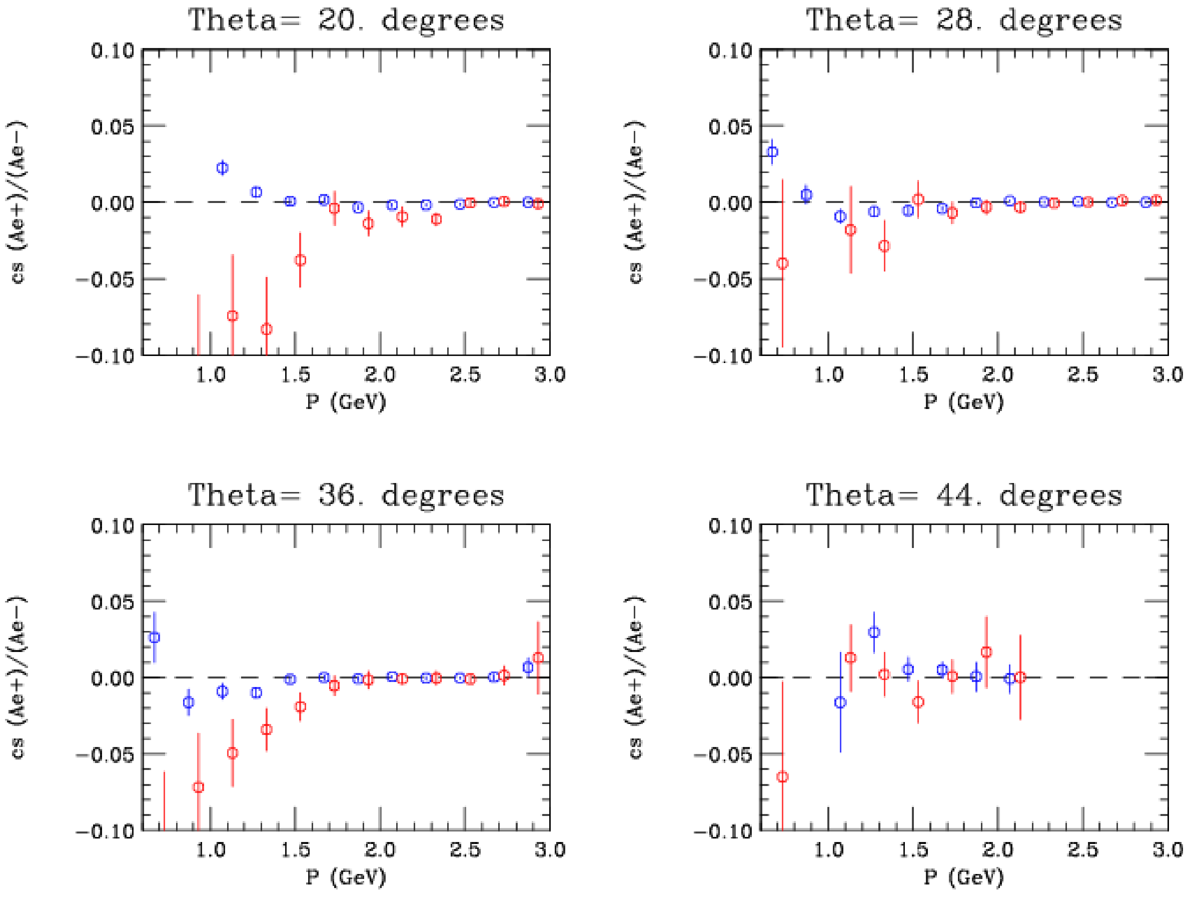

FIG. 22: Fractional contribution of the pair-symmetric asymmetry ($\frac{e^+_{rate}/e^-_{rate}}{e^+_{asym}/e^-_{asym}}$) as a function of momentum in four bins of scattering angle. The blue symbols are for NH_3, and the red symbols are for ND_3. In the final data analysis, only kinematic bins with $P > 1.2$ GeV are used.

G. Polarized nitrogen contribution c_1

The c_1 term in Eq. 2 accounts for the polarized nitrogen contribution to the measured double spin asymmetry. From the definition of the raw asymmetry in terms of the physics asymmetries of each of the polarizable nuclei in a target, it is straightforward to show that

$$c_1 = \frac{\eta_N}{\eta_{p,d}} \frac{A_N \sigma_N}{A_{p,d}\sigma_{p,d}} \frac{P_N}{P_{p,d}} \tag{11}$$

where η is the number of nuclei of a given species, σ is the cross section per nucleus, A is the double-spin asymmetry (hence $A\sigma$ is the cross section difference), and P is the polarization of a given material. For each of these four variables, the subscript N is for nitrogen-14, and (p, d) refers to either to proton (for the NH_3 target) or deuteron (for the ND_3 target). The first term $(\eta_N/\eta_{p,d})$ in Eq. 11 is 1/3, by definition, for ammonia.

In the nuclear shell model, the spin-1 nitrogen-14 nucleus can be considered as a spin-less carbon nucleus surrounded by an extra proton and neutron, each in a $1p_{\frac{1}{2}}$ orbital state [39]. After doing the spin projections, it turns out that the proton and neutron are each twice as likely to have their spin anti-aligned with the nitrogen spin, as having it aligned. It then follows that the second term in Eq. 11 can be evaluated using

$$A_N \sigma_N = -\frac{1}{3}(\sigma_p A_p + \sigma_n A_n) = -\frac{1}{3}\sigma_d A_d \tag{12}$$

where the subscript n refers to the neutron, and we have neglected the small d-state correction and used the relation $\sigma_d = \sigma_p + \sigma_n$. Inserting this into the second term of Eq. 11, we obtain a constant value of -0.33 ± 0.08 for the ND_3 target and $(-0.33 \pm 0.08)A_d/A_p$ for the NH_3 target. The uncertainty of 0.08 comes from an evaluation [40] of a range of more sophisticated treatments of the nitrogen wave function than the simple shell model.

The third term, the ratio of nitrogen to proton (deuteron) polarizations, can be evaluated using Equal Spin Temperature (EST) theory [38, 40]. This gives $p_N/P_p = 0.098$ for the average value $P_p = 0.77$ of this experiment. Experimental measurements from the SMC [40] are consistent with this result, although about 10% to 15% higher. We therefore used $P_N/P_p = 0.10 \pm 0.01$. The EST theory predicts $P_N/P_d = 0.48$, essentially independent of P_d. An experimental study at SLAC (E143 experiment, unpublished) yielded a much lower value of $P_N/P_d = 0.33$. We therefore used an average: $P_N/P_d = 0.40 \pm 0.08$.

Combining all these results together yields:

$$c_1^p = (-0.011 \pm 0.003)(\sigma_d/\sigma_p)(A_d/A_p) \tag{13}$$

$$c_1^d = -0.044 \pm 0.014 \tag{14}$$

To evaluate σ_d/σ_p, the ratio of deuteron to proton cross section per nucleus, we used recent fits to world data [20, 21]. To evaluate the ratio of double-spin asymmetries A_d/A_p we used a fit to world data that included the preliminary results of this experiment [41].

The results for c_1^p are shown as a function of x in several Q^2 bins in the left panel of Fig. 23, and vary between -0.003 at low x and Q^2 to -0.008 at the highest values of high x and Q^2.

For more details, see Ref. [46].

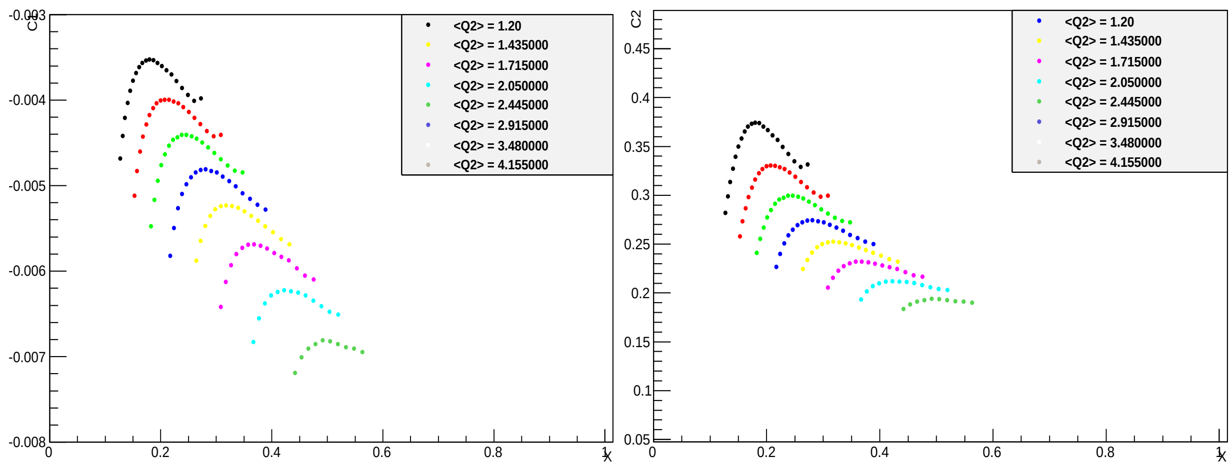

FIG. 23: Left panel: Correction factor c_1 for the proton as a function of x in several bins of Q^2; Right panel: c_2 for the deuteron for the in-bending portion of Part C.

H. Correction for NH_3 in ND_3

The c_2 term in Eq. 2 accounts for the polarized NH_3 contribution to the measured double spin asymmetry in the nominal ND_3 target. As discussed above, the ND_3 target contained an approximately 10.5% (by weight) admixture of NH_3 (or equivalent), and the protons in this material were polarized.

From the definition of $A_\|$, it is straightforward to show that

$$c_2 = \frac{\eta_p}{\eta_d}\frac{A_p \sigma_p}{A_d \sigma_d}\frac{P_p}{P_d} \tag{15}$$

where the symbols have the same meaning as in Eq. 11. The derivation of Eq. 15 is valid only if the dilution factor f in Eq. 2 is defined using the number of polarizable nucleons in deuterium only (not including the free protons), in the numerator of the ratio.

From the discussion above, the ratio of proton to deuteron nuclei is 0.105 ± 0.004 (0.120 ± 0.006) for the in-bending (out-bending) portion of Part C. The ratio of proton to deuteron polarizations is 2.31 ± 0.2 (2.15 ± 0.3) for the in-bending (out-bending) portion of Part C. Numerically, we then obtain:

$$c_2 = (0.24 \pm 0.024)\ \frac{A_p \sigma_p}{A_d \sigma_d} \qquad in - bending \tag{16}$$

$$c_2 = (0.26 \pm 0.038)\ \frac{A_p \sigma_p}{A_d \sigma_d} \qquad out - bending \tag{17}$$

To evaluate A_p/A_d and σ_p/σ_d, we used the same global fits as for c_1. The results for c_2 for Part C, in-bending polarity, are shown as a function of x in several Q^2 bins in the right panel of Fig. 23. They vary between 0.37 at low x and Q^2 and 0.16 at high x and Q^2.

I. Revised treatment of NH_3 in ND_3

The treatment of NH_3 in ND_3 in the above sub-section was originally used in our analysis, following the treatment of SLAC E143 and E155. Sebastian Kuhn pointed out in June 2013 that while a multiplicative correction may be suitable when the contamination is very small, it has three major flaws. The first is that it relies on a model of the asymmetry ratio, which may be inaccurate. The second is that the correction becomes infinitely large when the deuteron asymmetry model crosses zero. The third is that the statistical error does not accurately reflect that fluctuations in the measurements.

A more realistic treatment is to consider NH_3 as a background, and subtract its contribution. This is especially appropriate in the present experiment, where the proton asymmetry is well-measured at almost the same beam energy as for the deuteron. Equation 2 then becomes:

$$A_\parallel^d = \Big(\frac{N_1 - N_2 r_c}{N_1 + N_2 r_c} \frac{c_s}{f\ (1 + c_1)\ P_b\ P_t} - c_2' A_\parallel^p\Big)\ \frac{1}{f_{RC}} + A_{RC} \tag{18}$$

where $A_\parallel^p$ is the proton asymmetry, and the factor of c_2' differs from c_2 by the removal of the asymmetry ratio, thus:

$$c_2' = \frac{\eta_p}{\eta_d} \frac{P_p}{P_d} \tag{19}$$

Putting in the numerical values, we obtain

$$c_2' = (0.24 \pm 0.024) \qquad in - bending \tag{20}$$

$$c_2' = (0.26 \pm 0.038) \qquad\qquad out - bending \tag{21}$$

We used this revised method with the values of $A_\parallel^p$ determined from Part B. For consistency, we used the values with no radiative corrections applied to the proton.

The multiplicative and subtractive treatments are compared in Fig. 24, which shows the ratios of deuteron asymmetry divided by the world fit model, as a function of W, averaged over Q^2. The ratios tend to be a bit larger with the subtractive method, especially for $W > 2.3$ GeV. Note that the error bars with the subtractive method are larger by a factor of $(1 + c_1 + c_2)/(1 + c_1)$, or about 30%.

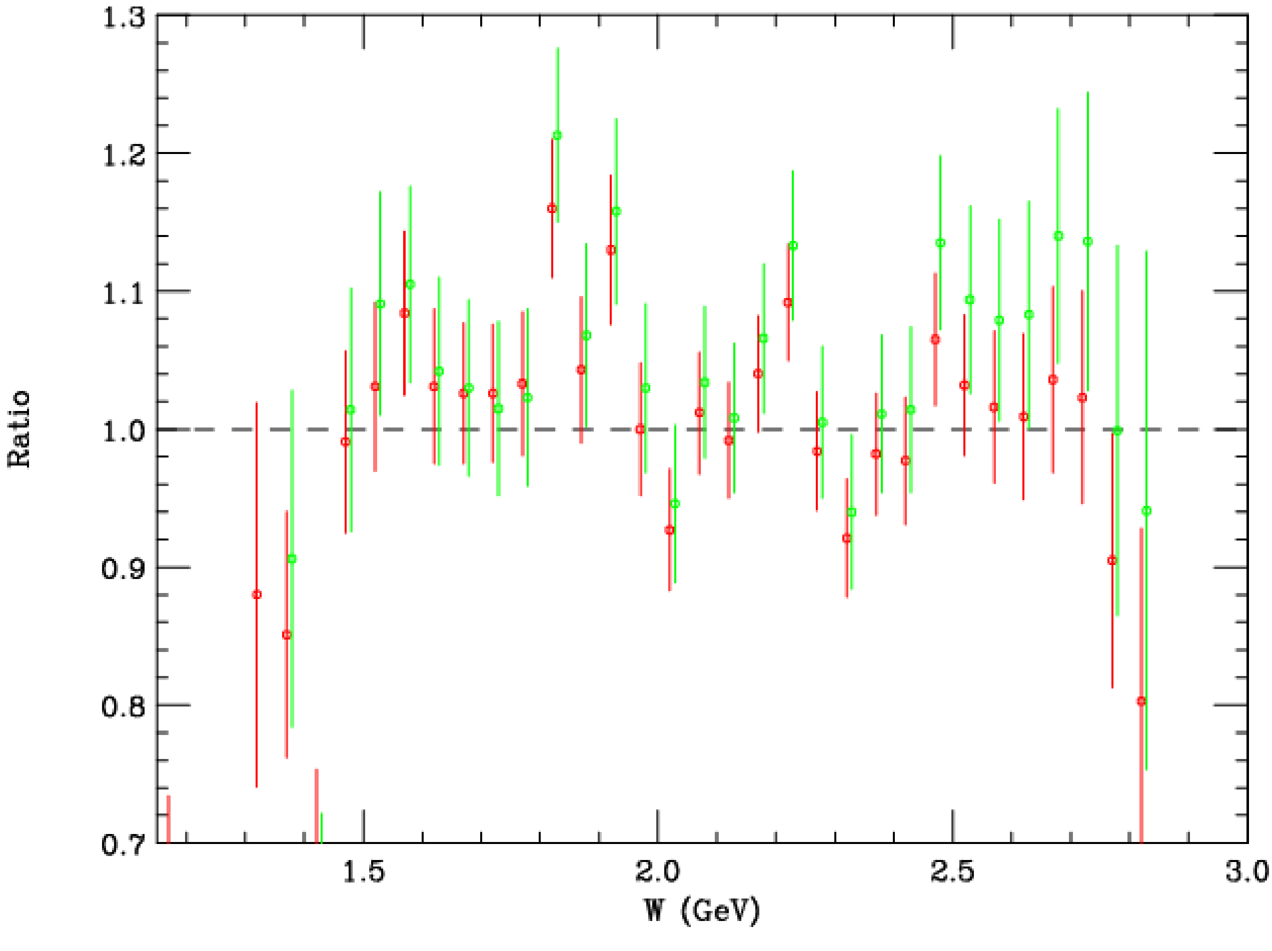

FIG. 24: Ratio of deuteron asymmetry divided by world fit, as a function of W, averaged over Q^2. The red points are with the original multiplicative correction for NH_3 in ND_3, while the green points (slightly shifted in W for clarity) are with the subtractive method.

The results shown in the next section all use the subtractive method.

J. Radiative corrections

In our analysis we approximate the scattering process as a one photon exchange, also called Born scattering. In reality, there are higher order processes contributing to the total measured cross sections and asymmetries. These effects are taken into account by calculating radiative corrections. The radiative corrections can be broken into 2 kinds: internal and external. The internal processes occur within the field of the scattering nucleus and consist of the vertex corrections (which effectively account for the running of the fine coupling "constant" $\alpha(Q^2)$), as well as the emission of hard photons from the incident or scattered electron. Some of the diagrams contributing to the internal correction are shown in Fig 25. External radiation occurs when a Bremsstrahlung photon is emitted from the incident electron prior to scattering (from a different nucleus from which the hard scattering takes place), or a hard photon is radiated by the scattered electron (see Fig 26). The probability of emitting a hard photon is approximately given by tdk/k, where t is the material thickness in radiation lengths, and k is the photon energy. An important consideration is that an electron is de-polarized by the emission of Bremsstrahlung photons. As a rough guide, internal radiation is "equivalent" to external radiation with t of order a few percent at JLab energies. The main difference between the two is that the electron angles are essentially unchanged in external radiation (characteristic angle m_e/E), while significant changes in the electron scattering at the vertex can occasionally occur in the internal radiation process. For our ammonia targets, the values of t relevant for external radiation are about 1.2%.

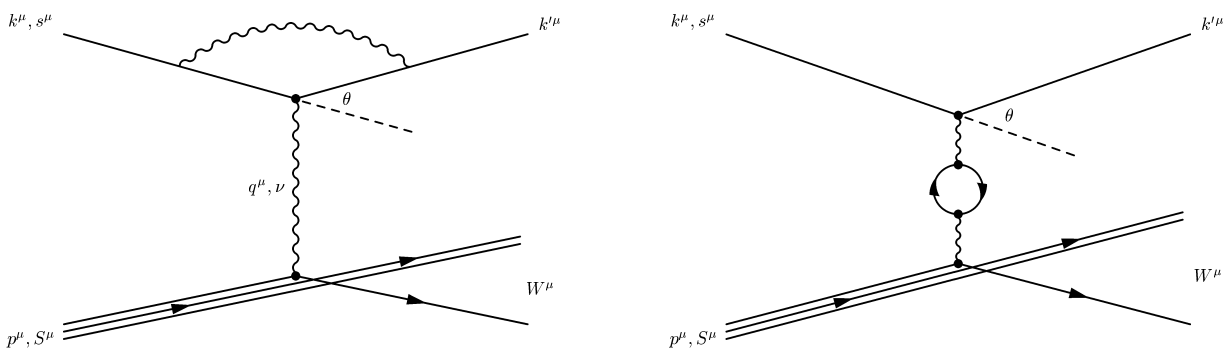

FIG. 25: Vertex correction and Vacuum polarization.

The radiative corrections require the evaluation of both polarized and unpolarized components for Born, internally radiated and fully radiated cross sections and asymmetries.

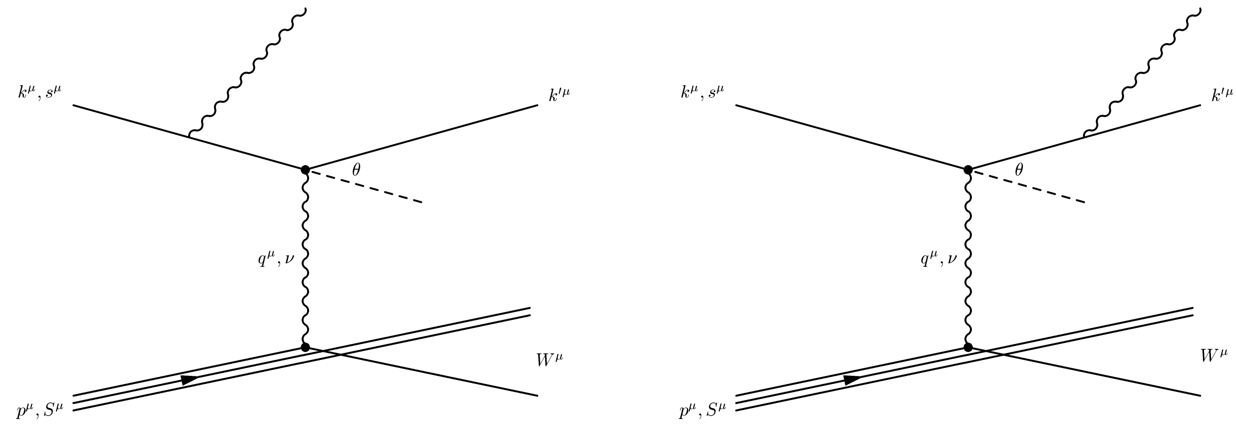

FIG. 26: Bremsstrahlung radiation by the electron before and after scattering.

Polarization-dependent internal radiative cross sections were calculated using the formalism developed by Kuchto and Shumeiko [43, 45]. External radiation was taken into account by convoluting internal radiative corrections with the a spectrum of incident electron energies, rather than a single monochromatic value, according to the formalism of Mo and Tsai [42]. The external radiation from the scattered electron was similarly taken into account.

The calculations were done with the computer code RCSLACPOL, developed for the E143 experiment at SLAC in the early 1990's [45]. The code requires input models for inelastic electron scattering as well as *ep* elastic (proton target) or *ep* and *en* quasi-elastic scattering. For spin-averaged inelastic cross sections, we used the recent fits to world data of Christy and Bosted [20] for the proton and Bosted and Christy [21] for the deuteron. Spin-dependent inelastic cross sections were obtained using a recent fit to JLab data (including the preliminary results of the present experiment) performed by N. Guler (to be published).

In our correction scheme, the radiative corrections are broken into an additive correction A_{RC} and a "radiative dilution factor" f_{RC}. The factor f_{RC} is nothing more than $(1 - f_e)$, where f_e is the fraction of events that have radiated down into a given (x, Q^2) bin from the *ep* elastic scattering process (or quasi-elastic process for the deuteron target). The factor A_{RC} accounts for all other radiative processes. The radiatively corrected asymmetry is then given by

$$A_{corr} = A_{uncorr}/f_{RC} - A_{RC} \tag{22}$$

The statistical error on the corrected asymmetry is given by

$$\delta A_{corr} = \delta A_{uncorr}/f_{RC} \tag{23}$$

Fig. 27 shows g_1/F_1 for the proton with and without radiative corrections as a function of W in bins of Q^2. The corrections are very small, corresponding to typical changes in g_1/F_1 of less than 1%. The largest effects are in the resonance region, where the asymmetry is changing rapidly with W. The error bars with radiative corrections applied are larger than without corrections, with the biggest increase at the largest W of a given Q^2 bin (corresponding to large values of y). The effect of radiative corrections for the deuteron is even smaller than for the proton. The effects are less pronounced in bins of (x, Q^2), as illustrated in Fig. 28.

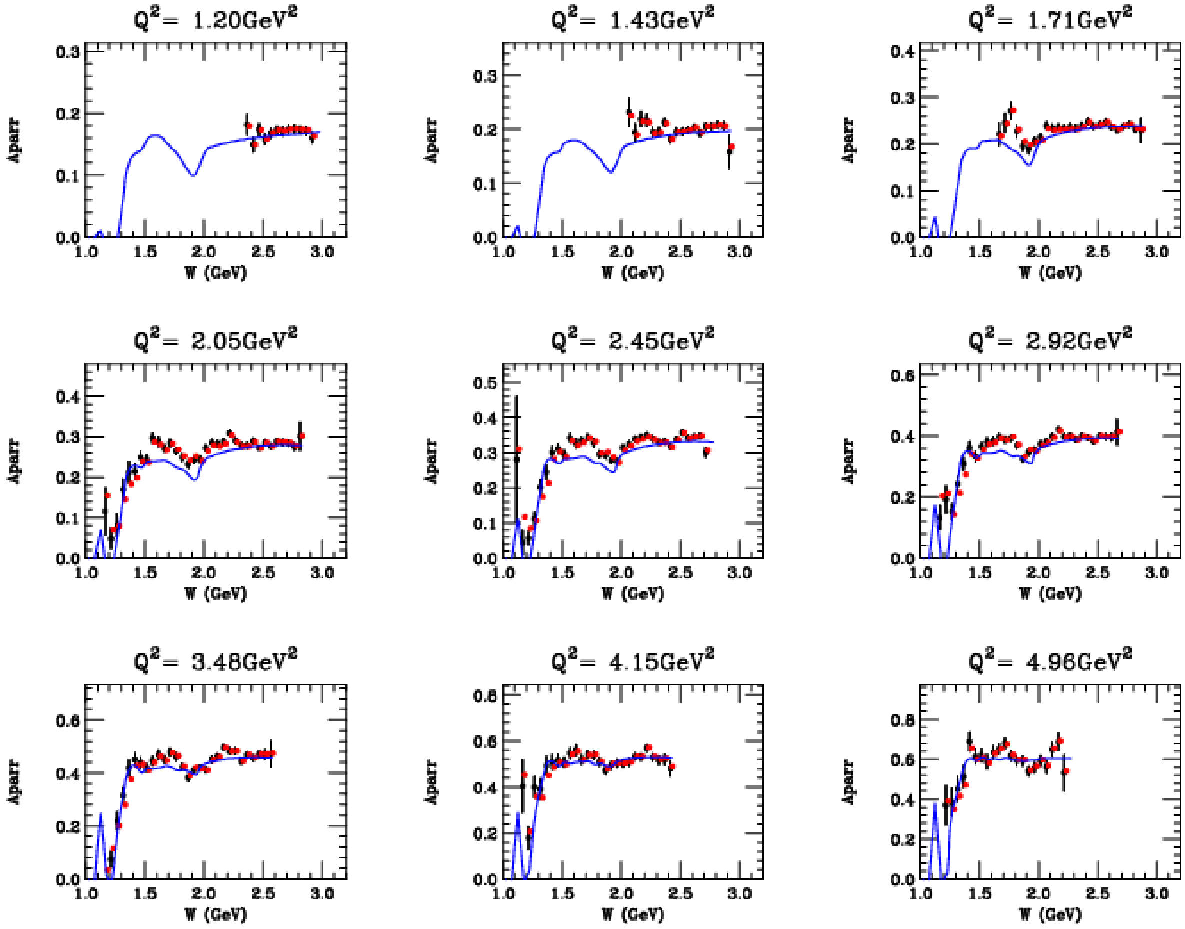

FIG. 27: Results for proton g_1/F_1 with (black points) and without (red points) radiative corrections applied. Results are shown in nine bins in Q^2, as a function of W.

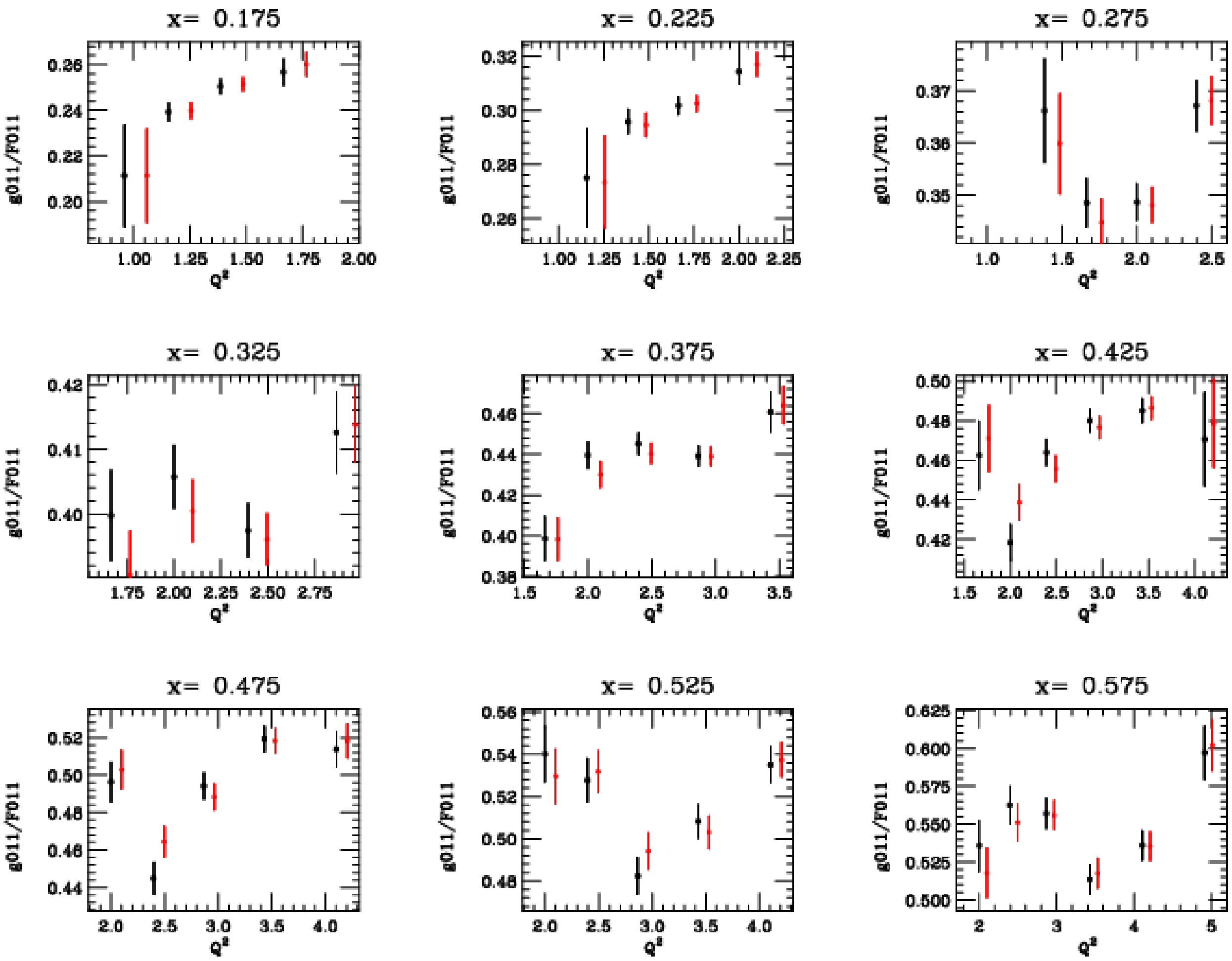

FIG. 28: Results for proton g_1/F_1 with (black points) and without (red points) radiative corrections applied. Results are shown in nine bins in X, as a function of Q^2.

IV. RESULTS FOR g_1/F_1

A. Results for g_1/F_1

In the one-photon-exchange (Born) approximation, the cross section for inclusive electron scattering with beam and target spin parallel ($\uparrow\Uparrow$) or anti-parallel ($\uparrow\Downarrow$) can be expressed in terms of the four structure functions F_1, F_2, g_1 and g_2, all of which can depend on ν and Q^2[41]:

$$\begin{aligned}\frac{d\sigma^{\uparrow\Downarrow/\uparrow\Uparrow}}{d\Omega dE'} &= \sigma_M \left[\frac{F_2}{\nu} + 2\tan^2\frac{\theta}{2}\frac{F_1}{M} \pm 2\tan^2\frac{\theta}{2}\right. \\ &\qquad \left.\times \left(\frac{E + E'\cos\theta}{M\nu}g_1 - \frac{Q^2}{M\nu^2}g_2\right)\right]\end{aligned} \tag{24}$$

where the Mott cross section is

$$\sigma_M = \frac{4E'^2\alpha^2\cos^2\frac{\theta}{2}}{Q^4}. \tag{25}$$

We can now define the double spin asymmetry $A_{||}$ as

$$A_{||}(\nu, Q^2, y) = \frac{d\sigma^{\uparrow\Downarrow} - d\sigma^{\uparrow\Uparrow}}{d\sigma^{\uparrow\Downarrow} + d\sigma^{\uparrow\Uparrow}}, \tag{26}$$

where $y = \frac{\nu}{E}$. Introducing the ratio R of longitudinal to transverse virtual photon absorption cross section,

$$R = \frac{\sigma_L(\gamma^*)}{\sigma_T(\gamma^*)} = \frac{F_2}{2xF_1}(1+\gamma^2) - 1, \tag{27}$$

where $\gamma = \frac{\sqrt{Q^2}}{\nu}$, we can define two additional quantities,

$$\eta = \frac{\epsilon\sqrt{Q^2}}{E - E'\epsilon} \tag{28}$$

and the "depolarization factor"

$$D = \frac{1 - E'\epsilon/E}{1 + \epsilon R} \tag{29}$$

which allow us to express $A_{||}$ in terms of the structure functions [41]:

$$\frac{A_{||}}{D} = (1 + \eta\gamma)\frac{g_1}{F_1} + [\gamma(\eta - \gamma)]\frac{g_2}{F_1}. \tag{30}$$

Here, $\epsilon = (1 + 2(1+\tau)(tan(\frac{\theta}{2}))^2)^{-1}$ and $\tau = \frac{\nu^2}{Q^2}$.

1. *Results for $A_{||}$*

The asymmetry $A_{||}$ was extracted from the raw data, as described in the previous Section, independently by P. Bosted and Y. Prok (Parts A and B) or N. Kvaltine (for Part C). The results were found to be in good agreement, as illustrated in Fig. 29 for Part B.

2. *Depolarization factor and R*

The depolarization factor, shown in Eq. 29, is an important factor in calculating $\frac{g_1}{F_1}$. This factor is a function of R, Eq. 27, which is the ratio of the longitudinal to transverse photon absorption cross-section. The values for these factors are supplied from an empirical fit to world data by Christy and Bosted [20]. The cross-section parametrization contained 75

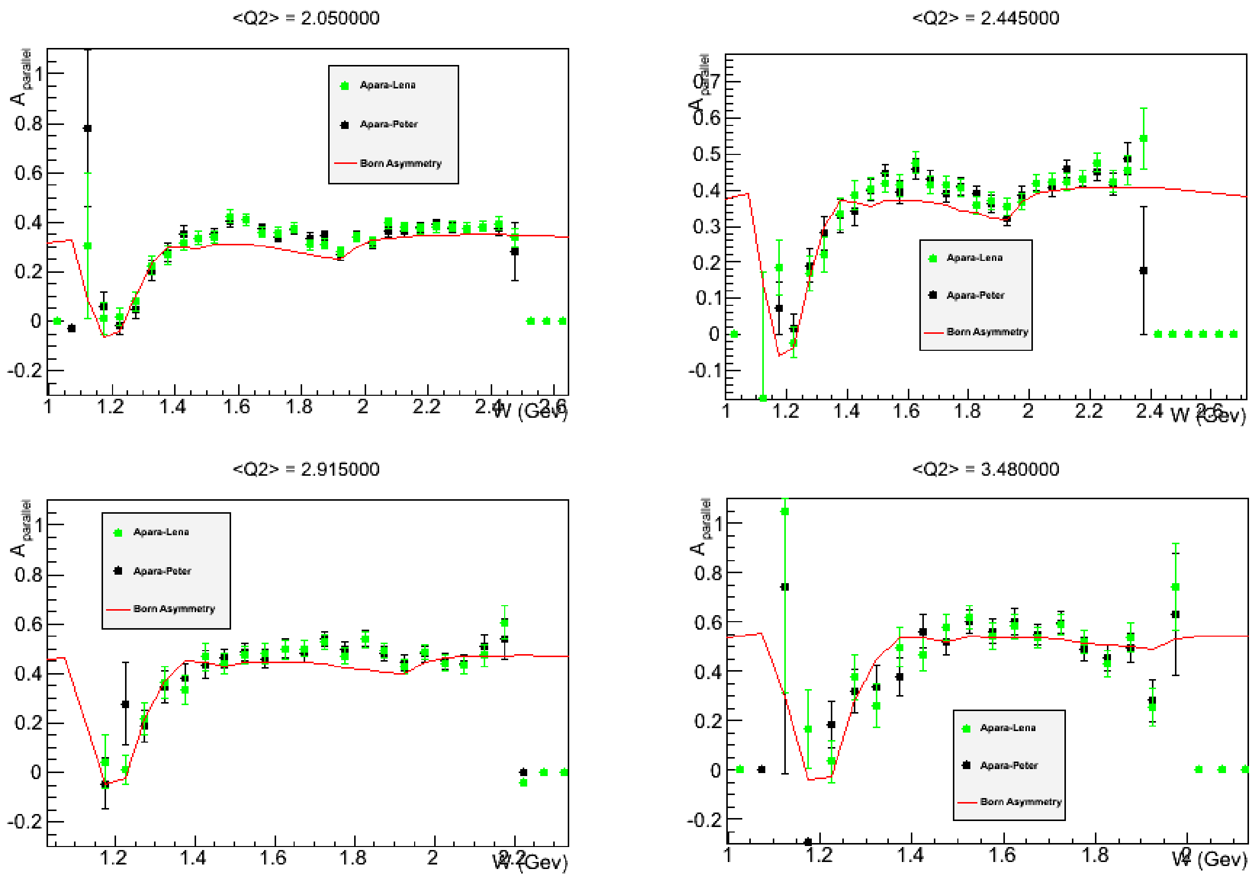

FIG. 29: Asymmetries $A_{||}$ as a function of W for several Q^2 bins for runs from Part B. Results from the analyses of P. Bosted (black points) and Y. Prok (green points) are in good agreement. The Born asymmetry model is depicted by the red curves.

free parameters; among them were parameters for the resonance masses and widths, non-resonance contributions, as well as transition form factors. The fit describes the data well over the range $0 \leq Q^2 \leq 8$ GeV^2 and $1.1 < W < 3.2$GeV which covers the area of interest for this study.

3. The g_2 correction

The measured asymmetry $A_{||}$ contains contributions from both the g_1 and g_2 structure functions. After some algebra, the equations can be re-written in the following form:

$$g_1/F_1 = (A_{||}/D')C_{g_2} \tag{31}$$

where the depolarization factor in this case (note that $D \neq D'$) is given by

$$D' = \frac{(1-\epsilon)(2-y)}{y(1+\epsilon R)} \tag{32}$$

and $y = \nu/E$. The g_2 correction factor is given by:

$$C_{g_2} = \frac{1+E'/E_0}{1+E'\cos(\theta)/E_0} \quad \frac{1}{1-2(g_2/g_1)Mx/[E_0+E'\cos(\theta)]} \tag{33}$$

To gauge the rough order of magnitude of the correction, we note that for $\cos(\theta) = 1$, $x = 0.5$, and our beam energy $E = 6$ GeV, then

$$C_{g_2} \approx 1 + (g_2/g_1)/10 \tag{34}$$

Since g_2 is smaller in magnitude than g_1, the overall correction differs by only a few percent from unity, as illustrated in Fig. 30.

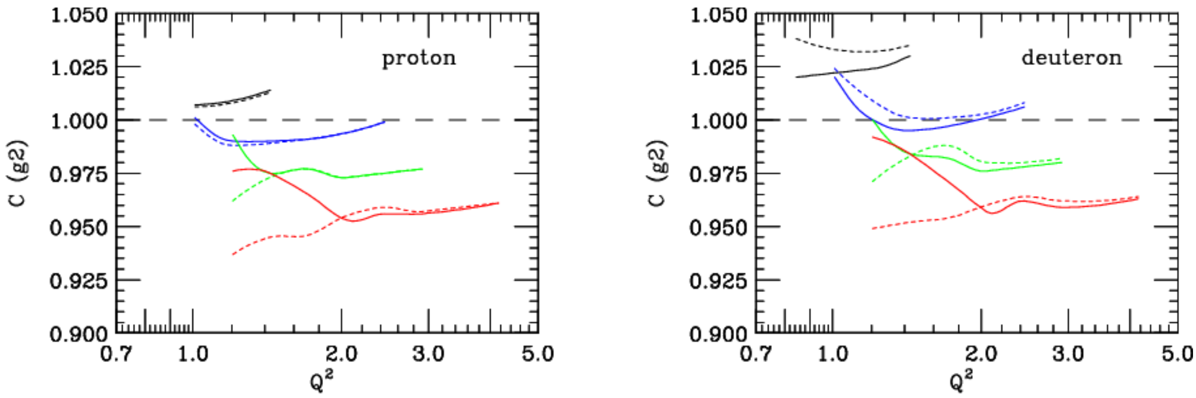

FIG. 30: Correction factor C_{g_2} as a function of Q^2 for $x = 0.225$ (black), $x = 0.325$ (blue), $x = 0.425$ (green), and $x = 0.525$ (red). The left panel is for the proton target and the right panel is for the deuteron. Dashed curves use the Wandzura and Wilczeck formula, while the solid curves use a fit to world data.

4. Combining data sets

Physics quantities that should depend only on (x, Q^2) (or equivalently (W, Q^2) were first calculated for each beam energy and torus polarity. These physics quantities were then combined, weighted by their statistical errors. The proton results used only Parts A and B, due to the very small amount of proton data in Part C. The deuteron data are from Part C only. Data from each of the individual run periods were compared with the corresponding averages, and found to be consistent within overall normalization uncertainties (dominated by the uncertainty in $P_B P_T$), as illustrated in Fig. 31 for the proton.

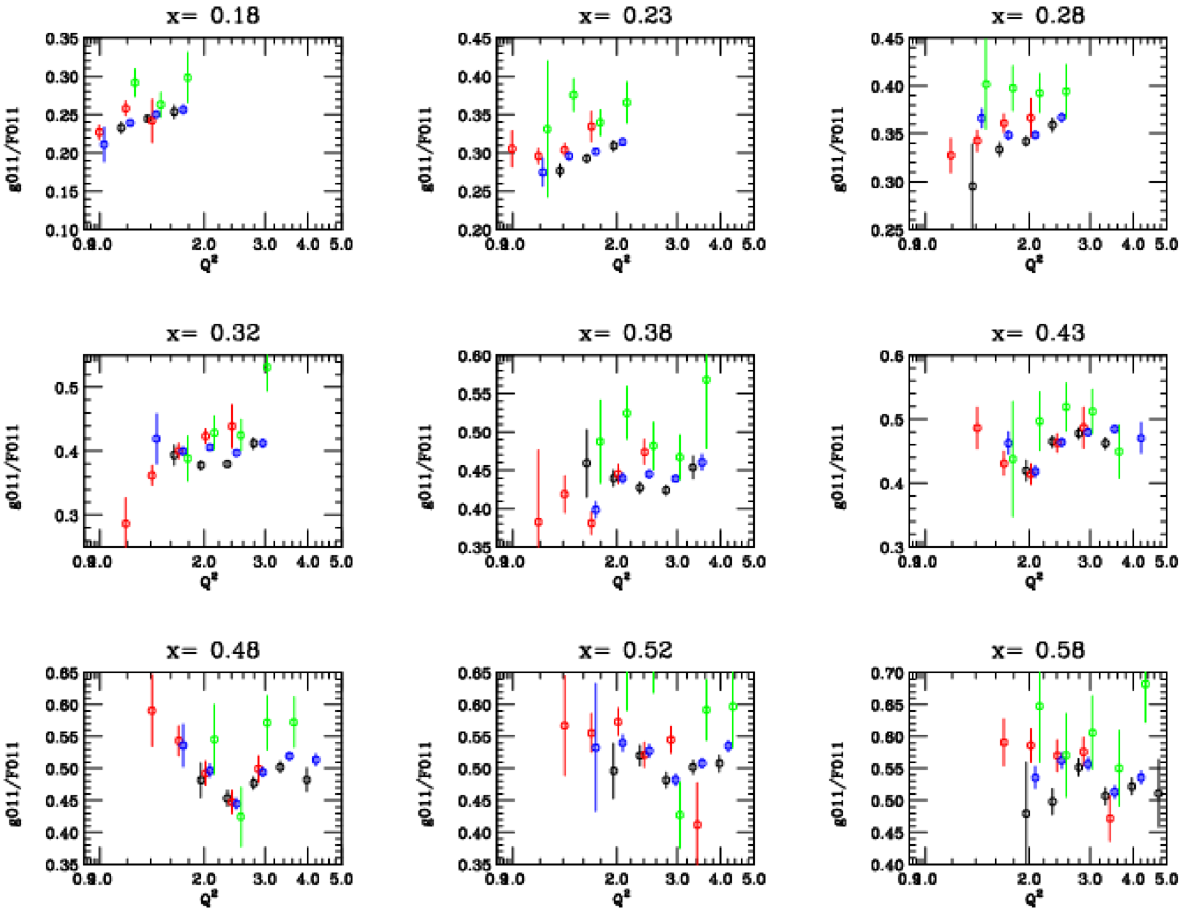

FIG. 31: Results for proton g_1/F_1 as a function of Q^2 in bins of x, for Part A with 5.9 GeV beam energy (black points), Part A with 4.8 GeV (red points), Part B with in-bending electrons (blue points), and Part B with out-bending electrons (green points). Only statical errors are shown. Different data sets are slightly offset in Q^2 for clarity.

B. Systematic error on $A_{\|}$

In this section we first summarize the systematic error on $A_{\|}$ arising from each of the terms in Eq. 2. We then discuss the systematic error from three other additional sources, which were assumed to be negligible in Eq. 2.

1. *Beam charge ratio f_c*

The uncertainty in the ratio of incident beam charge for positive and negative helicities (relative to the target polarization direction) was much less than 0.0001. This negligibly small value was achieved by three methods: 1) frequent reversal of the half-wave plate; 2) keeping the charge asymmetry less than 0.1% using an on-line feedback system; 3) generating beam helicity buckets in pairs.

2. *Dilution factor f*

The dilution factor is one of the two most important sources of systematic error in the determination of $A_{\parallel}$. There are a number of factors which contribute to this error:

- The ammonia length l_A has an estimated relative uncertainty of 3% for most of the experiment (except 5% for the begining of part A), based on the spread in the individual determinations for pairs of carbon and ammonia runs, combined with an overall uncertainty of 1% in the carbon target areal density.
- The distance between the "banjo" windows, L (which determines how much helium there is in the target), has an estimated uncertainty of 0.2 cm, based on inconsistencies between the determination of 2.0 cm from the empty target runs, and 2.3 cm for a direct measurement in the lab when the target was at room temperature.
- The areal density of the aluminum "banjo" beam windows has an estimated uncertainty of 0.005 gm/cm^2 (a relative error of 10%).
- The areal density of the target Kapton windows has an estimated uncertainty of 0.005 gm/cm^2 (a relative error of 5%)
- Approximately 3% uncertainties in the density of ammonia and helium at 1 K.

Folding together these uncertainties for our particular target (i.e. about 70% ammonia by areal density, 30% other nuclei), the result is a 1.5% relative error in f, with no significant (x, Q^2) dependence for $W > 1.4$ GeV.

While all of the above contributions vanish in the limit of a pure ammonia target, there is still the overall scale uncertainty in the ratios of spin-averaged inclusive cross sections $\sigma_p/\sigma_{14}N$ and σ_d/σ_{14N}. Based on the fluctuations between various experiments fit in Refs. [20–22], we estimate the uncertainties be 1.5% in both cases. Combining this with the target-parameter-dependent uncertainty of 1.5%, the total relative uncertainty in f is 2.3%

3. *Product of beam and target polarization P_BP_T*

For the proton, the relative error on P_BP_T has a statistical component of 1% (for Parts A and B combined). The P_BP_T analysis was done independently by four individuals: each picking their own optimum set of cuts. For in-bending Part B (which is by far the most important case), the average values were: 0.645 ± 0.007 (Peter B.); 0.648 ± 0.006 (Andrey Kim); 0.646 ± 0.008 (Angela B.); and 0.650 ± 0.006 (Silva P.). Similarly small differences were found for Part A. We therefore conservatively estimate a further systematic error of 1% coming from the choice of cuts and model for G_E/G_M. The net systematic error on P_BP_T for the proton is therefore 1.4%.

As a final "sanity check", we compared the the results from P_BP_T from ep elastic, to those obtained from NMR measurements of P_T and Møller measurements of P_B. The results were; 1.5% higher for Part A (6 GeV); 2% lower for Part A (4.8 GeV); and 4% higher for Part B. These are well within the approximately 3 to 4% NMR P_T polarimetry error, and the estimated 4% error on Møller measurements of P_T. The errors on NMR and Møller could have been reduced with more frequent and longer TE measurements for NMR, and more frequent Møller measurements under a variety of conditions, but this effort was not made because it would have reduced the time available for production data collection.

For the deuteron, we estimate an overall normalization error of 3 - 5% in the target polarization values extracted from the cold NMR signals by the double-peak method, for polarization values above 30%, as discussed in Ref. [49]. This uncertainty includes the sensitivity to the baseline subtraction, and choice of polynomial order. Our procedure of using the good-fit high polarization double-peak values to normalize the NMR areas, and hence obtain the target polarization at lower polarization values (where the double-peak method does not work as well), introduces an additional systematic error of order 3%. The net result is an estimated systematic error of 5% on the run-averaged target polarization values for the in-bending and out-bending portions of Part C. The systematic error on the beam polarization from the Møller methods is estimated to be 4%, based on comparison with more accurate measurements made in Halls A and C over a period of many years. The net result is an overall relative systematic error of 7% in $P_B P_T$ for the deuteron.

As a check, we obtained $P_B P_T$ from quasi-elastic ep scattering. The statistical accuracy was reduced from what we would have like by the necessity of placing cuts against ep elastic from the free protons in the target. The results were: $P_B P_T = 0.206 \pm 0.021$ for the in-bending runs (compared to 0.214 ± 0.015 from NMR/Møller); and $P_B P_T = 0.307 \pm 0.036$ for the out-bending runs (compared to 0.235 ± 0.017 from NMR/Møller), where the quasi-elastic errors are purely statistical. The out-bending error is considerably bigger than the in-bending one, due to the factor of two less running in this configuration.

4. Error on pair-symmetric and mis-identified pion correction

Recall that $c_s - 1$ is defined as ratio of e^+/e^-, as shown in Fig. 21. The correction is negligibly small for $P < 2$ GeV ($y < 0.65$), but rises to values as large as $c_s - 1 = 0.10$ at $P = 1.2$ ($y = 0.8$), the lowest value of P used in the analysis. Based on the disagreement between our two measurements (both particles in-bending, or both out-bending), we assign a systematic error of 30% on $c_s - 1$, corresponding to a systematic error of up to 3% on $A_\parallel$ at the highest values of y.

We assumed that the pair-symmetric asymmetry was zero in Eq. 2, which is consistent with the results shown in Fig. 22. However, at low P, there are some indications that the scaled contribution could be as large as 1% for $1.2 < P < 1.5$ GeV for the proton, and as much as 3% for the deuteron. We therefore assigned a relative systematic error of 1% (3%) to $A_\parallel$ for the proton (deuteron) for $P < 1.5$ GeV.

5. Radiative corrections

As shown in Fig. 28, the application of radiative corrections make typically less than 1% changes to g_1/F_1. To study the systematic error, radiative corrections were calculated with several alternate cross section and asymmetry models. No significant changes were observed, at the 0.5% level.

6. Error on c_1

As discussed in section III G, the error on c_1 is estimated to be 0.003 (0.014) for the proton (deuteron), independent of (x, Q^2).

7. Error from the c_2' term

Following the discussion in Section III I, the systematic error on c_2' is 0.025 (0.038) for the in-bending (out-bending) deuteron runs, independent of (x, Q^2). The corresponding relative uncertainty in the deuteron asymmetries and structure functions is given by $0.025(A_\parallel^p/A_\parallel^d)$ for the inbending runs, and $0.038(A_\parallel^p/A_\parallel^d)$, where the ratio $A_\parallel^p/A_\parallel^d$ varies between about 2 and 3 over the (x, Q^2) range of this experiment.

8. Detection efficiency

In Eq. 2, it was assumed that the detector efficiency was the same for target and beam polarization aligned or anti-aligned. A correction should be made if the overall particle rate is higher for one state than the other (i.e. raw $A_\parallel \neq 0$), resulting in a rate-dependence to the detection efficiency. To estimate the size of this correction, we first measured the detector efficiency as a function of total particle rate, averaged over helicity, by varying the beam current. As illustrated in Fig. 32, the rate of good electrons divided by beam current is not flat, but instead shows a slight decrease with increasing beam current. The slope corresponds to a 1% decrease in detection efficiency per nA of beam current. At the nominal beam current of the experiment, 7 nA, this corresponds to a 0.07% decrease in detector efficiency for every 1% increase in total particle rate. If the total particle rate were entirely good electrons, the measured asymmetry would be 7% lower than if the detector efficiency were not rate-dependent. Fortunately, the total particle rate is dominated by photo-produced pions. Using the pre-scaled un-biased hardware trigger as a guide, we found that over 90% of particles in the detectors are pions. From measurements at SLAC [54] and our own measurements of the pair-symmetric asymmetry (dominated by π^0 photoproduction, see above), it is known that the raw asymmetry in pion production is an order-of-magnitude smaller than for electron scattering. Therefore the correction would be of order 0.7%. Taking into account that approximately the same correction applies to *ep* elastic scattering (from which we determine $P_B P_T$), the net effect on the final electron asymmetry is reduced even further. We therefor made no correction for rate-dependent detection efficiency, and assign an overall systematic error of 0.7%.

As a further check, we measured the deficiency slope in four bins of scattering angle θ. We found the slope to be only about 20% bigger at large angles than small angles.

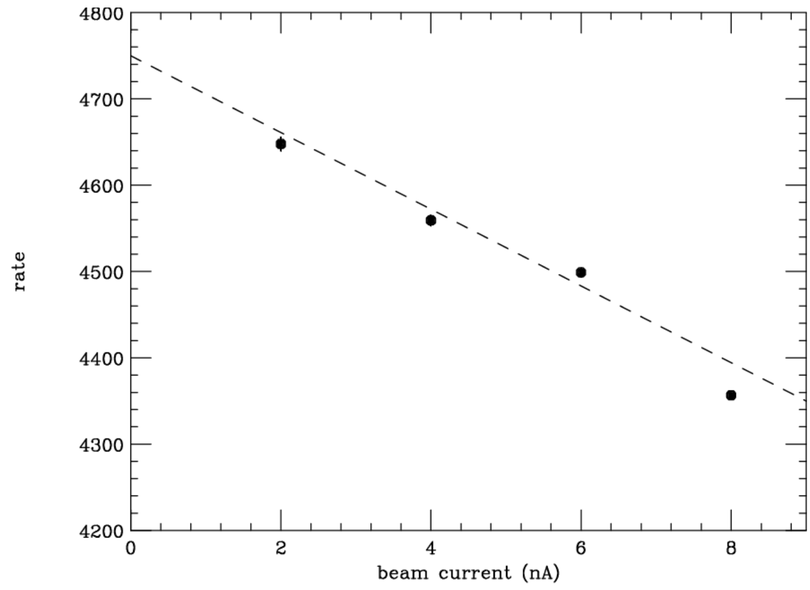

FIG. 32: Good electron rate (counts divided by Faraday Cup reading) from the carbon target as a function of nominal beam current. The dashed line is a linear fit.

9. Parity-violating background

The raw asymmetry arising due to eN parity-violating inelastic scattering from any of the nucleons in the target is given to a good approximation by $A_{\parallel}^{PV} = P_B Q^2 [0.8 \times 10^{-4}]$, independent of x (from Particle Data Book). Since $A_{\parallel}^{PV}$ does not depend on target polarization P_T, (unlike the double spin asymmetry $A_{\parallel}$), the contribution to $A_{\parallel}$ cancels, by definition, for equal running times with the target polarization aligned (denoted by t^+) or anti-aligned (t^-) with the beam direction. For un-equal running times, the contribution from $A_{\parallel}^{PV}$ is reduced by a factor $r_T = (t^+ - t^-)/(t^+ + t^-)$. Averaged over the entire experiment, $r_T = 0.04$ for NH_3 and $r_T = 0.11$ for ND_3. Since the measured raw double-spin raw asymmetry is approximately given by $Q^2 \times 10^{-2}$ for our average virtual photon energy $\nu = 3$ GeV, the relative parity-violating contribution was less than 0.1% in all (x, Q^2) bins, and was neglected.

10. *Summary of systematic error on* $A_{\parallel}$

Taking all the above errors in quadrature, the overall relative systematic error on $A_{\parallel}$ has an (x, Q^2)-independent value of 2.8% for the proton, and 8.1% for the deuteron. The proton error is dominated by the uncertainty in f, while the deuteron is dominated by the uncertainty in $P_B P_T$. The only systematic error that depends strongly on kinematic values is the pair-symmetric correction, which increases the overall error to 4.1% (8.6%) for the proton (deuteron) at $y = 0.8$.

C. Systematic error on g_1/F_1

As can be seen in Eq. 31, the systematic error on g_1/F_1 has two additional sources of error compared to $A_{\parallel}$: the error on D' (dominated by the uncertainty in R), and the error on the g_2 correction. Since the knowledge of R and g_2 may improve in the future, we list the values we used in the final results table.

1. *Error on* D'

The dominant error in D' comes from the uncertainty in R (since $\frac{dD'}{D'} = \epsilon dR$). Fortunately, relatively recent precision data from JLab have reduced the overall uncertainty in R in the kinematic region of the present experiment from about 0.10 to 0.03 (see Ref. [20]). Since $0.4 < \epsilon < 0.9$ for the present experiment, the uncertainty in R introduces a relative error of 1% to 3% in g_1/F_1. Another source of error in D' comes from the estimated systematic uncertainty in beam energy of 10 MeV, in electron momentum P of about $0.002P$, and in scattering angle θ of about 0.5 mr. Taken together, these result in a relative uncertainty in D' of 0.5% to 1%, with the largest uncertainty at large y.

2. *Error on* g_2 *correction*

The values of g_2/g_1 used in the analysis were taken from a fit to world data [52]. In order to estimate the systematic error on the correction, we also used the assumption that there are no deviations from the twist-two model of Wandzura and Wilczeck (g_2^{WW}) [53]

$$g_2(x, Q^2) = -g_1(x, Q^2) + \int_x^1 g_1(\xi, Q^2)d\xi/\xi \tag{35}$$

From this relation, it can be seen that the relative size of the g_2 correction is insensitive to the overall scale of g_1, and depends only on the x-dependence of g_1 at higher x. The corrections C_{g_2} using only the Wandzura and Wilczeck contribution are shown as the dashed curves in Fig. 30. The difference from the world fit of Ref. [52] are quite small, except for $x = 0.525$ at low Q^2, which corresponds to the low-W end of the resonance region. We estimated the systematic error on the g_2 correction to be half of the difference between the two models for g_2.

3. *Summary of systematic errors*

A summary of systematic uncertainty factors contributing to $\Delta A_\parallel$ is presented in Table V.

Factor	Proton	Deuteron
f	2.3%	2.3%
$P_b P_t$	1.4%	7.0%
c_s	0-3%	0-3%
c_1	0.3%	1.4%
$c_2'(A_p/A_d)$	0%	5-10%
$R.C.$	0.5%	0.5%
r_c	0.1%	0.1%

TABLE V: A summary of systematic uncertainty factors contributing to $\Delta A_\parallel$ for both targets. Uncertainty is given as a percentage error on $\Delta A_\parallel$.

D. Physics results

The essential physics results from this analysis are the ratios g_1/F_1 for the proton and deuteron. These can be examined as a function of W to look for resonance structure, and as a function of x to study QCD evolution.

1. g_1/F_1 as a function of W

The results for g_1/F_1 as a function of W are shown for the proton in nine bins of Q^2 in Fig. 33. The systematic error bands are dominated by an overall normalization uncertainty common to all points. The results are in reasonably good agreement with the published results from the Eg1b experiment [6], but have considerably higher statistical precision. The eg1b results are on average a few percent lower than the present results, which is well within the overall systematic error of the two experiments. The higher precision of the present results clearly shows some structure near $W = 1.9$ GeV, similar to the fit to previous world data [52], shown as the solid curves. The strength of the structure near $W = 1.9$ GeV seems to decrease with increasing Q^2. The strength of the structure appears to be less strong than in the published eg1b data. As shown in Fig. 28, this is not due to radiative corrections, which are very small near $W = 2$ GeV. It is possible that the difference is due to the dilution factor, because the published eg1b analysis did not have the high-accuracy empirical fits to world data that are available today.

Another observation is that the strong peak near $W = 1.5$ GeV seems to be under-represented in the fit, especially at moderate values of Q^2. This may indicate that the strength of the important $S_{11}(1530)$ resonance is under-estimated.

The results for the deuteron are shown in Fig. 34. The comparison to the world data fit (dominated by eg1b results) is reasonably good. Again, the large peak near $W = 1.5$ GeV is somewhat larger in the data than the fit. The dip near $W = 1.9$ GeV is not as clearly seen as for the proton, in part due to the considerably larger errors for the deuteron target.

2. Results for g_1/F_1 as a function of Q^2

The results for g_1/F_1 as a function of Q^2 are shown for the proton in nine bins of x in Fig. 35. The systematic error bands are dominated by an overall normalization uncertainty common to all points. Small bin-centering corrections have been applied to the data: typically these are only significant in the highest and lowest Q^2 bins in each panel.

The results are in reasonable agreement with the published results from the Eg1b experiment [6], as represented by the black curves that resulted from a fit to those data. Nonetheless, significant deviations of order 10% relative can be seen in certain kinematic

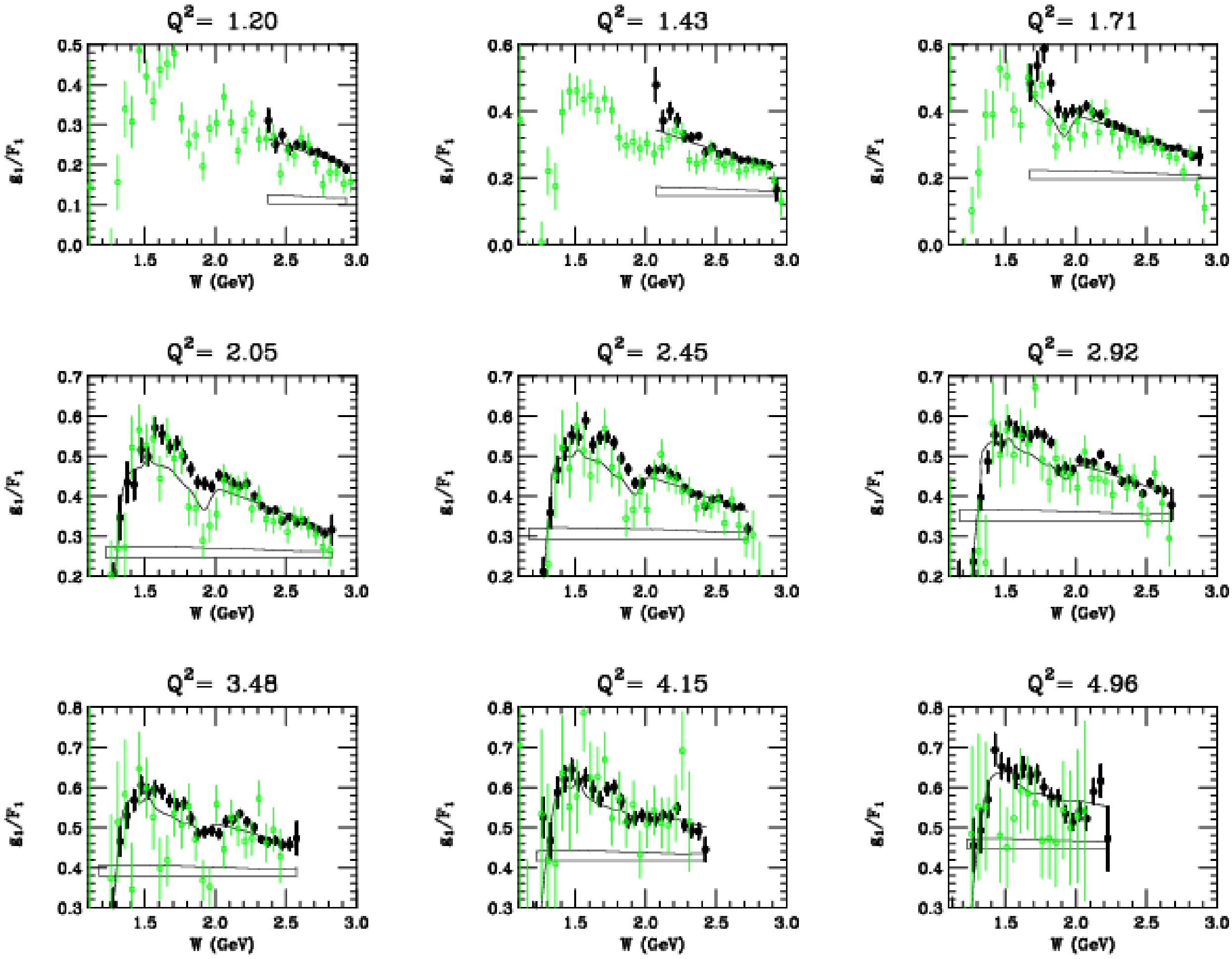

FIG. 33: Results for g_1/F_1 as a function of W for the proton in nine bins of Q^2. The present results are the black solid points, and the published eg1b results are in green. The curves are the fit to previous data used for radiative and other corrections. The bands at the bottom of each panel represent the total systematic error (point-to-point as well as overall normalization errors combined.) Note the offset from 0 in the vertical axis of most of the panels.

regions, especially at lower values of W and Q^2. For reference $W = 2$ is indicated by an arrow in each panel. As seen previously, there is significant resonance structure in the data for $W < 2$ GeV. The data are completely consistent with higher Q^2 data from SLAC [1, 2], shown as the green points.

The blue and red curves are pQCD calculations from the LSS group [51] with positive δG (blue curves) and negative δG (red curves). In each case, higher twist coefficients were fit to give the best agreement with the data available in 2007. The difference in overall magnitude between the curves is of the same order or larger than our experimental error bars. However,

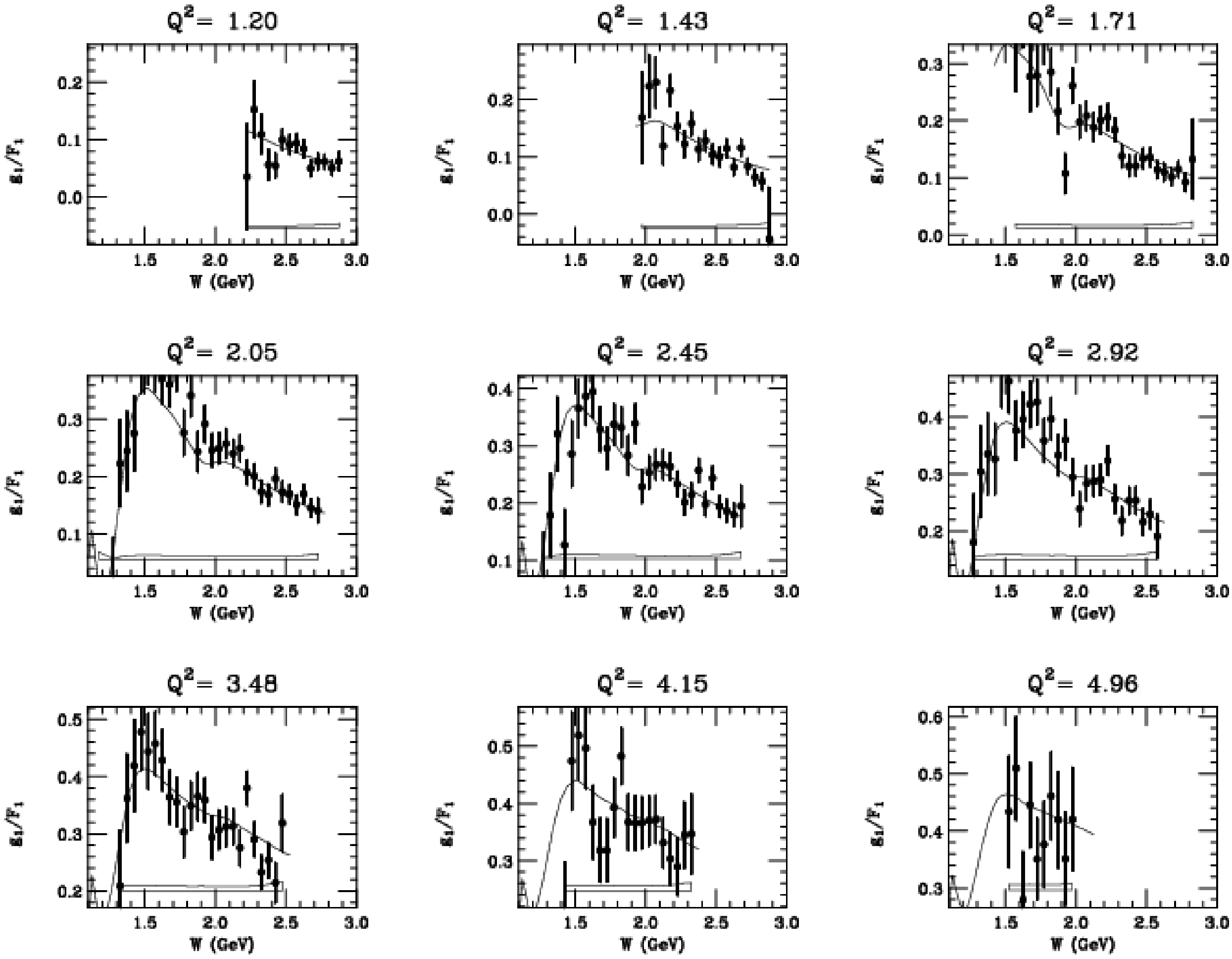

FIG. 34: Same as Fig. 33 except for the deuteron. Data from eg1b are not shown, for clarity.

the Q^2-dependence is generally larger than in the data, and the magnitude of the curves is above the data at low x, and below at higher x. Nonetheless, it appears that the curves with negative δG agree better with the flat Q^2-dependence of our data than the positive δG curves. A new global pQCD fit that includes our new data should be able to significantly improve the determination of higher twist corrections, and start to shed light on $\delta G(x)$.

The results for the deuteron are shown in Fig. 36. The results are in good agreement with previous results from Eg1b [6] and SLAC [1, 2]. The data are also reasonably consistent with the fit used for radiative and other corrections (black curves) as well as the two pQCD calculations from LSS [51]. As is the case for the proton, the present data show less Q^2-dependence than either model, and are completely consistent with no Q^2-dependence at all for $W > 2$ GeV.

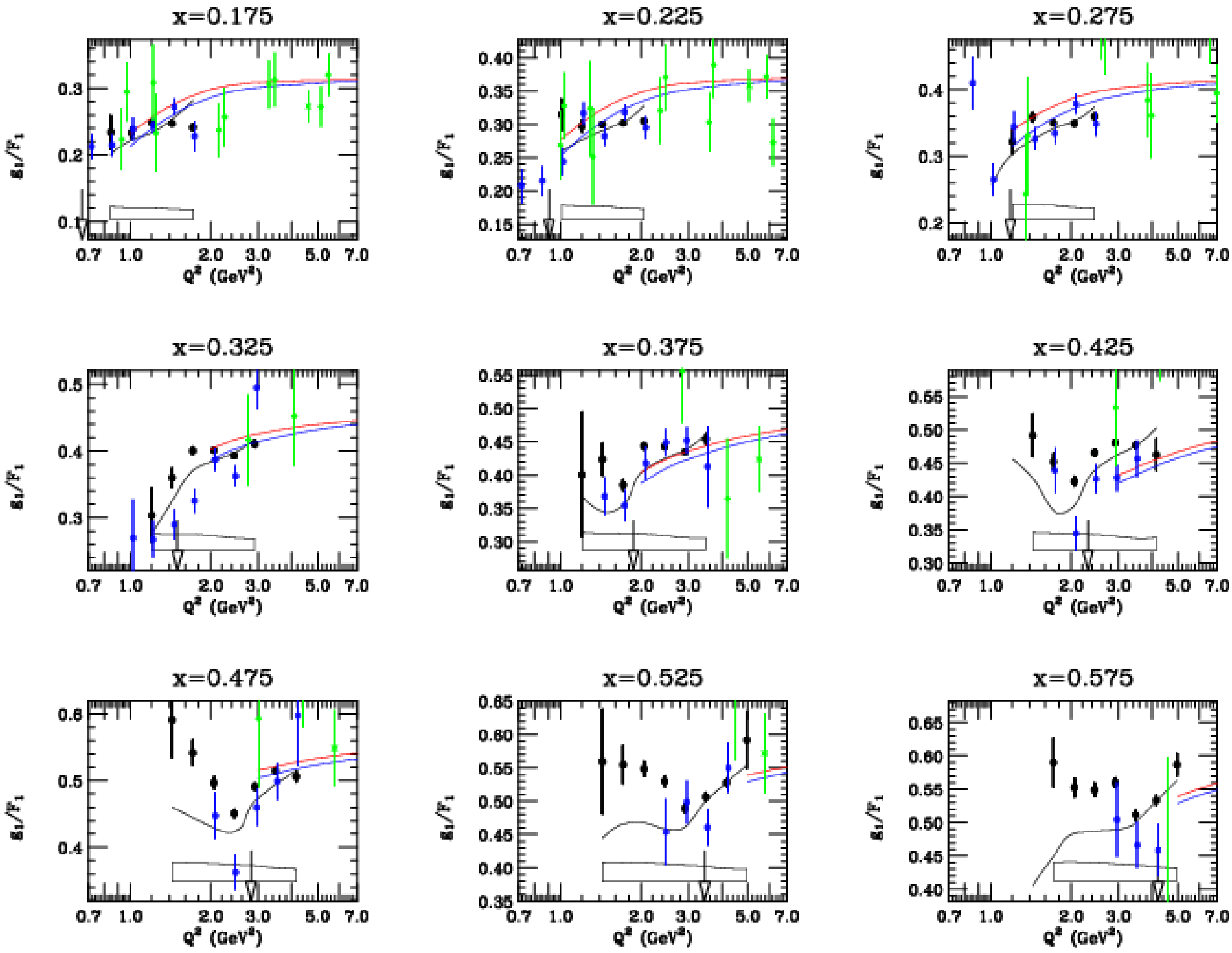

FIG. 35: Results for g_1/F_1 as a function of Q^2 for the proton in nine bins of x. The present results are the black solid points, the JLab eg1b results [6] are the blue points, and the results from SLAC [1, 2] are shown in green. The arrows correspond to $W = 2$ GeV. The black curves are the fit to previous data. The bands at the bottom of each panel represent the total systematic error (point-to-point as well as overall normalization errors combined). The blue and red curves are representative pQCD calculation from the LSS group with two models for gluon polarization (positive and negative, respectively).

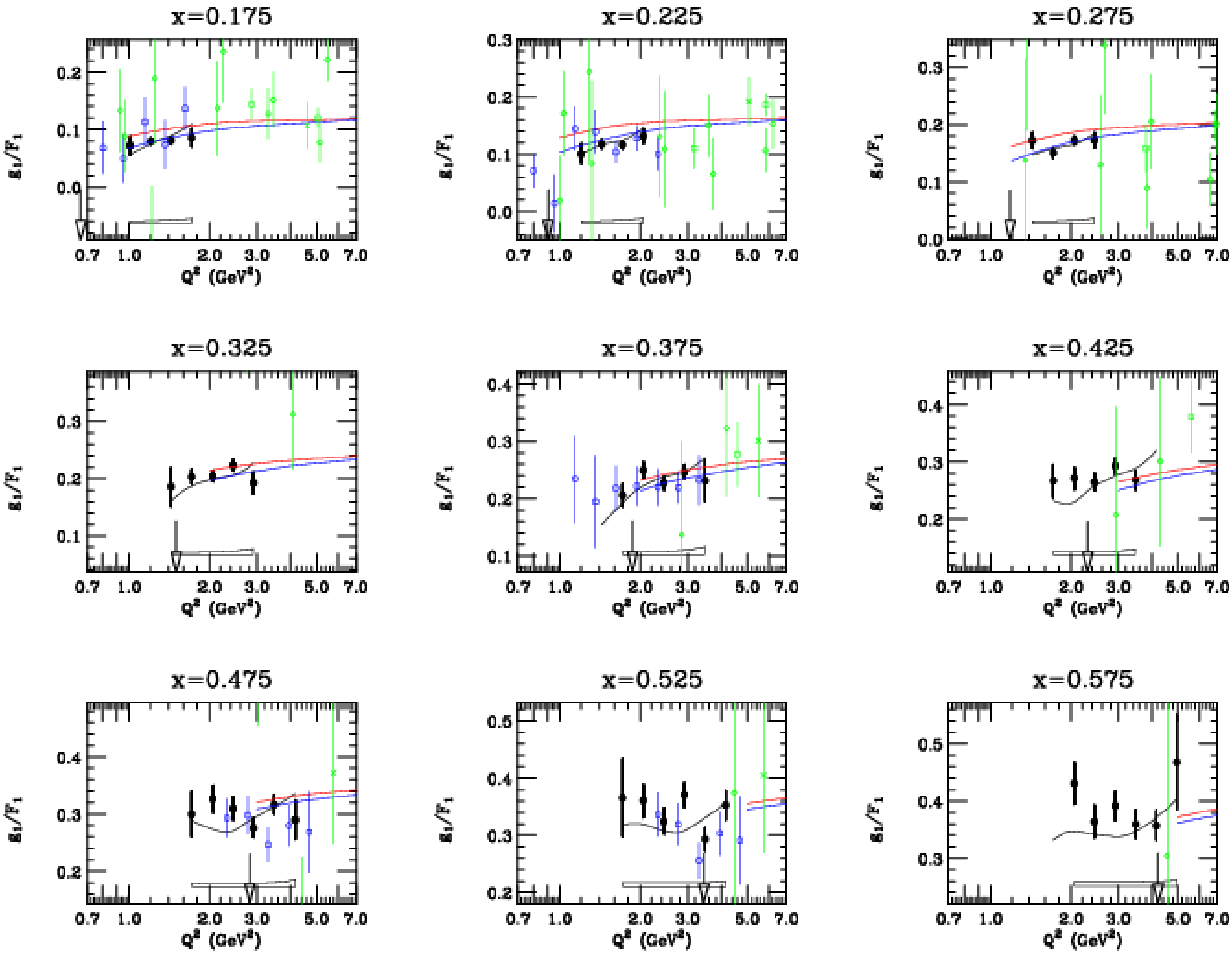

FIG. 36: Same as Fig. 35 except for the deuteron. The green points include results from COMPASS [4], HERMES [3], and SLAC [1, 2].

V. CONCLUSION

A very careful and meticulous analysis of inclusive electron scattering from polarized protons and deuterons was performed using the eg1-dvcs data set. The data quality was found to be excellent for the proton target, and a big improvement in both statistical and systematic uncertainties was achieved in the kinematic region probed, compared to previous experiments. The deuteron results also show a considerable improvement over previous data.

The most striking result is the almost complete lack of any significant Q^2-dependence in the ratio g_1/F_1 for $W > 2$ GeV and $0.15 < x < 0.5$. The results provide important constraints to global pQCD fits to inclusive nucleon structure functions, and pave the way to a larger reach in Q^2 and x with higher energy beams in the future.

---

[1] SLAC E143, K. Abe *et al.,* Phys. Rev. Lett. 74 (1995) 346; Phys. Rev. Lett. 75 (1995) 25; Phys. Lett. B364 (1995) 61; Phys. Rev. D58, 112003 (1998).

[2] SLAC E155, P. L. Anthony *et al.,* Phys. Lett. B463 (1999) 339.

[3] HERMES, A. Airapetian *et al.,* Phys. Lett. B442 (1998) 484; Phys. Lett. B404 (1997) 383; hep-ex/0609039 (submitted to Phys. Rev. D).

[4] COMPASS, V. Y. Alexakhin *et al.*, hep-ex/0609038 (submitted to Phys. Lett. B); E. S. Ageev *et al.*, Phys. Lett. B **612**, 154 (2005).

[5] R. Fatemi *et al.* [CLAS Collaboration], Phys. Rev. Lett. **91**, 222002 (2003) [arXiv:nucl-ex/0306019].

[6] K. V. Dharmawardane *et al.* [CLAS Collaboration], Y. Prok *et al.* [CLAS Collaboration], Phys. Lett. B **672**, 12 (2009) [arXiv:0802.2232 [nucl-ex]].

[7] V. N. Gribov and L. N. Lipatov, Sov. J. Nucl. Phys. 15 (1972) 438, 675; Yu. L. Dokshitzer, Sov. Phys. JETP 46 (1977) 641; G. Altarelli and G. Parisi, Nucl. Phys. B126 (1977) 298.

[8] C.D. Keith *et al.,* Nucl. Instr. Meth. **501**, 327 (2003).

[9] "Determination of the Banjo and Ammonia Lengths from Event Rates", Eg1-dvcs TN08: http://www.jlab.org/Hall-B/secure/eg1-dvcs/technotes/LandLAv2/LandLA.pdf

[10] B.A. Mecking, *et al.*, Nucl. Instr. Meth., **503**, 513 (2003).

[11] "Drift Chamber Alignment", Eg1-dvcs TN10: http://www.jlab.org/Hall-B/secure/eg1-

dvcs/technotes/DCAlign/DCAlign.pdf

[12] http://clasweb.jlab.org/rungroups/eg1-dvcs/wiki/index.php/Drift_Chamber_Calibration

[13] https://userweb.jlab.org/ ungaro/maureepage/proj/Cerenkov/cc_periods/eg1dvcs.html

[14] "Beam Position (x,y) and Target Center (z) from Raster ADCs,", Eg1-dvcs TN02: http://wwwold.jlab.org/Hall-B/secure/eg1-dvcs/technotes/raster.pdf

[15] "N-tuple 22", Eg1-dvcs TN07: http://wwwold.jlab.org/Hall-B/secure/eg1-dvcs/technotes/nt22/nt22.pdf

[16] "racking from Drift Chambers to Target Solenoid", Eg1-dvcs TN04: http://wwwold.jlab.org/Hall-B/secure/eg1-dvcs/technotes/targetinfo/target_info.pdf

[17] "Helicity-dependence of Faraday cup information and delayed helicity corrections for EG1-DVCS data sets", Eg1-dvcs TN01: http://wwwold.jlab.org/Hall-B/secure/eg1-dvcs/technotes/FCandHel/FCandHelicity.pdf

[18] "New way of doing Cherenkov Mirror Matching", Eg1-dvcs TN12: http://wwwold.jlab.org/Hall-B/secure/eg1-dvcs/technotes/ccc2/ccc2.pdf

[19] Eg1-dvcs TN13: "Fiducial Cuts based on IC Shielding", by Peter Bosted: http://wwwold.jlab.org/Hall-B/secure/eg1-dvcs/technotes/fidcutic/fidic.pdf

[20] M.E. Christy and P.E. Bosted, "Empirical Fit to Precision Inclusive Electron-Proton Cross Sections in the Resonance Region", accepted in Phys. Rev. C 81, 055213 (2010). (arXiv:0712.3731)

[21] P.E. Bosted and M.E. Christy, Phys. Rev. C 77, 065206 (2008). (arXiv:0711.0159).

[22] P.E. Bosted and V. Mamyan, [arXiv:1203.2262] (2012).

[23] Eg1-dvcs TN05: http://wwwold.jlab.org/Hall-B/secure/eg1-dvcs/technotes/radcor/radcor.pdf

[24] Eg1-dvcs TN17: http://wwwold.jlab.org/Hall-B/secure/eg1-dvcs/hind/hind.pdf

[25] Eg1-dvcs TN17 prime: http://www.jlab.org/Hall-B/secure/eg1-dvcs/technotes/hind/hindSuman.pdf

[26] Eg1-dvcs TN06: http://wwwold.jlab.org/Hall-B/secure/eg1-dvcs/technotes/eleceff/eleceff.pdf

[27] Eg1-dvcs TN03: http://wwwold.jlab.org/Hall-B/secure/eg1-dvcs/technotes/energy/energy.pdf

[28] Eg1-dvcs TN09: http://wwwold.jlab.org/Hall-B/secure/eg1-

dvcs/technotes/rastercheck/rasterTN.pdf

[29] Eg1-dvcs TN22: http://wwwold.jlab.org/Hall-B/secure/eg1-dvcs/technotes/BadFileList/BadFileList.pdf

[30] Eg1-dvcs TN11: http://wwwold.jlab.org/Hall-B/secure/eg1-dvcs/technotes/momcorr/momcorr.pdf

[31] A. Puckett et al., Phys. Rev. Lett 104(24):242301 (2010).

[32] L. Andivahis, P. Bosted *et al.,* Phys. Rev. D50, 5491 (1994)

[33] Eg1-dvcs TN15: http://www.jlab.org/Hall-B/secure/eg1-dvcs/technotes/deuteronTargetCalibration/Deu

[34] D. G. Crabb and W. Meyer. "Solid Polarized Targets for Nuclear and Particle Physics Experiments." Annu.Rev.Nucl.Part.Sci. **47** 67 (1997).

[35] O.A. Rondon. "Corrections to nucleon spin structure asymmetries measured on nuclear polarized targets." Phys. Rev. C 60 035201 (1999).

[36] B. Adeva *et al.* [The Spin Muon Collaboration],"Measurement of Proton and Nitrogen Polarization in Ammonia and a Test of Equal Spin Temperature" Nucl. Instr. Meth. **A 419** 60 (1998).

[37] J.M. Blatt and V.F. Weisskopf, *Theoretical Nuclear Physics* (Dover Publication Inc., New york, 1979

[38] D. G. Crabb and W. Meyer, Annu. Rev. Nucl. Part. Sci. **47** 67 (1997).

[39] O.A. Rondon. Phys. Rev. C 60 035201 (1999).

[40] B. Adeva *et al.* [The Spin Muon Collaboration], Nucl. Instrum. Meth. A 419 60 (1998).

[41] R.G. Fersch *et al.,* [The CLAS Collaboration], to be published.

[42] L.W. Mo, Y.S. Tsai *Radiative Corrections to Elastic and Inelastic ep and νp Scattering*, Reviews of Modern Physics **41/1**,(1969)

[43] T.V. Kuchto and N.M. Shumeiko *Radiative effects in deep inelastic scattering of polarized*

leptons by polarized nucleons, Nuclear Physics **B219**,412-436(1983)

[44] Gregory S. Mitchell *A precision measurement of the spin structure function* $g_1(x, Q^2)$ *for the proton and deuteron*, PhD Thesis, 2000

[45] K.Abe *Measurements of the proton and deuteron structure functions*, Phys.Rev. **D58:112003** (1998)

[46] Eg1-dvcs TN14: http://www.jlab.org/Hall-B/secure/eg1-dvcs/yprok/n14/n14note.pdf

[47] D. Wiser, PhD thesis, University of Wisconsin, 1977 (unpublished).

[48] P. Bosted, *Pair-Symmetric and Pion Backgrounds for EG1b*, CLAS-NOTE 2004-2005.

[49] Dulya, C. M. "A Line-Shape Analysis for Spin-1 NMR Signals", Nuc. Inst. Meth. A, 398. pp. 109-125.

[50] Bosted, P. http://clasweb.jlab.org/rungroups/eg1-dvcs/wiki/index.php/Even_ newer_ IC_ shaadow_ cut% 2C_ and_ new_ track_ quality_ cut

[51] E. Leader, A. V. Sidorov and D. B. Stamenov, Phys. Rev. D **73**, 034023 (2006).

[52] N. Guler, S. Kuhn *et al.,* to be published.

[53] S. Wandzura and F. Wilczek, Phys. Lett. B72 (1977)195.

[54] The E155 Collaboration, P.L. Anthony *et al.,* Phys. Lett. B458, 536 (1999).